

Simulation of Luminosity Monitoring with LUCID in ATLAS

September 11, 2009

Abstract

Monte Carlo simulations are used to characterize the response of LUCID and its performance as a luminosity monitoring system. All results are obtained with a light LUCID geometry made of 32 (instead of 40) Cerenkov tubes read out by photo-multipliers.

The performance of LUCID is evaluated with 9159 single pp inelastic collision events generated with PHOJET at $\sqrt{s} = 14$ TeV and passed through a GEANT3-GCALOR simulation of the full ATLAS detector.

When the number of pp interactions per event is less than 2, a method based on counting empty events gives an accuracy of 2%. Hit counting can be used for any μ smaller than 25 with an accuracy of 6%. The accuracy of all methods can be improved by increasing the size of the Monte Carlo calibration sample.

CONTENTS

Contents

1	Introduction	3
2	Detector description	4
2.1	Cerenkov light emission	5
2.2	Light propagation and detection	7
3	Response to a single particle	8
3.1	Signal from on-axis pions	8
3.2	Signal from off-axis pions	9
3.3	Signal from off-axis photons	10
4	Response to pp collisions	11
4.1	Event generator	11
4.2	Track propagation inside ATLAS	13
4.3	The LUCID volume	13
4.4	Definition of the particle direction	15
4.5	Track propagation inside LUCID	16
4.6	Photo-electron spectrum	16
4.7	Hit definition	16
4.8	Time of flight	17
4.9	Angle with the beam	17
4.10	Energy	18
5	Study of luminosity monitoring algorithms	19
5.1	Definition of the type of detected pp interaction	20
5.2	Detection efficiency and hit distribution	21
5.3	Simulation of high luminosity events	22
5.4	Counting methods	23
5.5	Linear extrapolation model	24
5.6	Combinatorial model	26
5.7	Polynomial fit model	30
6	Conclusions and summary	32
A	Wavelength dependent parameters	33
B	Counting empty events	35
C	Counting particles in coincidence mode	38
D	From hits to particles	42

1 Introduction

1 Introduction

An general introduction to the plans for luminosity measurement at LHC is reported in [?]. A study of luminosity monitoring in ATLAS with a toy Monte Carlo simulation is reported in [?]. This note presents the performance of LUCID [?] as an ATLAS luminosity monitoring system.

Given a physical process with cross section σ , the average bunch luminosity (\mathcal{L}_{BX}) is the ratio between the average number of processes per event¹ (μ) and the corresponding cross section:

$$\mathcal{L}_{BX} = \frac{\mu}{\sigma} \quad (1)$$

The task of a luminosity monitor is to provide an estimate of luminosity at any value of μ . The average bunch luminosity can be converted to the instantaneous luminosity (L) by using the bunch crossing frequency ($f_{rev} = 40$ MHz), the maximum number of bunches around LHC (3564) and the number of circulating filled bunches (n_{BX}):

$$L = \mathcal{L}_{BX} \times f_{rev} \times \frac{n_{BX}}{3564}. \quad (2)$$

Luminosity monitors in ATLAS are asked to cover a wide range of luminosities, from $L = 10^{27} \text{ cm}^{-2}\text{s}^{-1}$ to $L = 10^{34} \text{ cm}^{-2}\text{s}^{-1}$ (LHC design luminosity). Assuming $\sigma_{inel} = 80$ mb, the expected number of inelastic pp interactions per event at design luminosity ($n_{BX} = 2808$) is $\mu \sim 25$.

At the lowest luminosity, the ALFA detector [?] will measure absolute luminosity from elastically scattered protons with a predicted accuracy of about 3%. A less precise measurement (10 – 20% accuracy) is foreseen with special beam conditions by measuring the beam transverse dimensions (“beam separation scan”).

For the purpose of luminosity monitoring, two type of event samples can be defined. A **calibration sample** is defined by the fact that the probability of having events with overlapping pp interactions is negligible ($\mu \ll 1$). This sample is needed to calibrate the detector by evaluating the response to a single pp interaction. A **measurement sample** is any other event sample in which a monitor is asked to measure the luminosity.

The note is divided in two parts. The first part illustrates the geometrical description of LUCID (Section 2) and the study of the detector response (Sections 3 and 4). In the second part (Sections 5), Monte Carlo simulations of the full ATLAS detector are used to study the performance of LUCID as a luminosity monitoring system. The average number of pp interaction per event is extracted from the measurement samples in a wide range of luminosities with several methods and the results are compared with the expected values.

¹An event is defined as a crossing between two filled bunches.

2 Detector description

2 Detector description

LUCID consists of two detector modules located at a distance of about 17 m from the pp interaction point (IP). Each module is made of twenty aluminum tubes surrounding the beam pipe and pointing at the IP (see Figure 1).

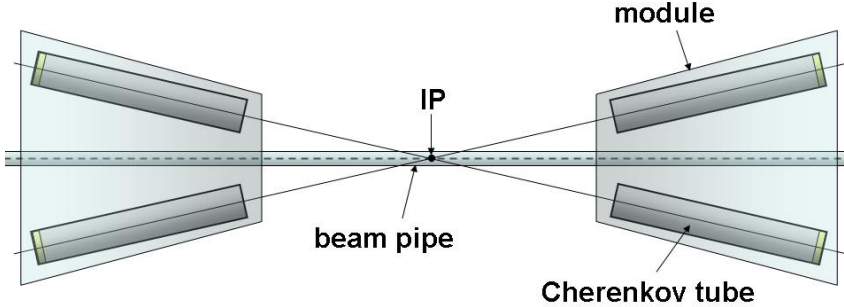


Figure 1. Schematic view of the pointing geometry of four LUCID tubes (not in scale).

Tubes are located in a pressure tight aluminum vessel which contains a Cerenkov gas radiator (C_4F_{10} at 1.1 bar). Two rings of 8 tubes per module are directly coupled to photo-multipliers (Hamamatsu R762), while four tubes per module are read-out via optical fibers. A water based cooling system keeps the vessel temperature below the PMT critical value (50° Celsius) during the beam-pipe bake-out operations.

A realistic simulation of the main LUCID detector elements (vessel, radiator, tubes, optical surfaces, PMTs and cooling system) has been developed in a stand-alone GEANT4 [?] simulation (version 4.7.1p01). A sketch of the geometrical description of a single Cerenkov tube is shown in Figure 2.

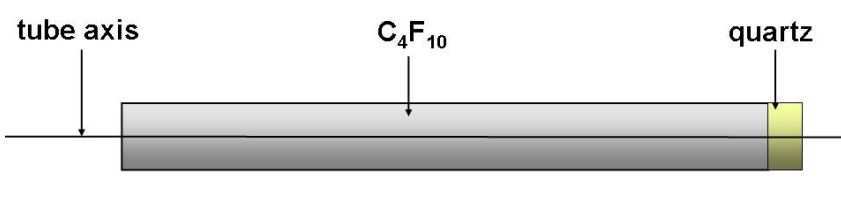


Figure 2. Geometrical description of the Cerenkov tube (not in scale).

The PMT is simulated with a thin quartz disc matching the transversal dimension of the tube. The photo-cathode and the chain of dynodes inside the PMT are not simulated. A photon crossing the surface of the window is detected with a probability corresponding to the quantum efficiency provided by Hamamatsu [?]. The simulation of the PMT quartz window is crucial since it acts as a photon emitter, in addition to the main gas radiator. All parameters used to describe the detector geometry are listed in Table 1.

2.1 Cerenkov light emission

Distance from the IP [mm]	16715.5
Vessel length [mm]	1532
Vessel inner radius [mm]	85
Vessel outer radius [mm]	125.15 (min), 147 (max)
Vessel inner thickness [mm]	2.5
Vessel outer thickness [mm]	3.0
Vessel bulkhead thickness [mm]	3.2
Cooling radius [mm]	78
Cooling thickness [mm]	2
Radial distance Tube-Beam [mm]	96.3 (ring1)
Radial distance Tube-Beam [mm]	114.7 (ring2)
Tube thickness [mm]	1.0
Tube length [mm]	1495
Tube radius [mm]	7.0
Pmt thickness [mm]	1.2
Pmt radius [mm]	7.0
Gas pressure [bar]	1.1
Gas temperature [kelvin]	293.15

Table 1. Parameters used for the geometrical description of LUCID.

2.1 Cerenkov light emission

Cerenkov light is emitted when a charged particle traverses a material with a velocity v larger than the speed of light in the medium c/n :

$$v > \frac{c}{n} \rightarrow \beta = \frac{v}{c} > \frac{1}{n} \quad (3)$$

where n is the refractive index of the radiator. A basic description of Cerenkov light emission can be found in [?]. The minimal velocity at which the emission takes place is c/n and corresponds to a particle energy threshold E_{th} such that:

$$E_{th} = \gamma m_0 c^2 = \frac{m_0 c^2}{\sqrt{1 - \left(\frac{v}{c}\right)^2}} = \frac{m_0 c^2}{\sqrt{1 - \left(\frac{1}{n}\right)^2}} \quad (4)$$

where m_0 is the rest mass of the particle. For π in C_4F_{10} (quartz), E_{th} is 2700 MeV (190 MeV). For e in C_4F_{10} (quartz), E_{th} is 9.3 MeV (0.7 MeV).

2.1 Cerenkov light emission

The emission angle θ_C is a function of the refractive index of the medium and of the particle velocity:

$$\cos \theta_C = \frac{1}{\beta n}. \quad (5)$$

The refractive index of a gas is a function of the emitted photon energy (E), the pressure (P) and the temperature (T) of the gas [?]. In case of C_4F_{10} :

$$n = \sqrt{\frac{2x+1}{1-x}}, \text{ where } x = \frac{0.25938 \times P[\text{bar}]}{T[\text{kelvin}]} \frac{1}{1 - \left(\frac{E[\text{eV}]}{17.0}\right)^2}. \quad (6)$$

The refractive index of quartz is calculated with the Sellmeier equation [?]:

$$n = 1 + \sqrt{\frac{46.41}{10.666^2 - E^2[\text{eV}]} + \frac{228.71}{18.125^2 - E^2[\text{eV}]} + \frac{0.014}{0.125^2 - E^2[\text{eV}]}}. \quad (7)$$

The refractive index of C_4F_{10} and quartz are shown in Figure 3.

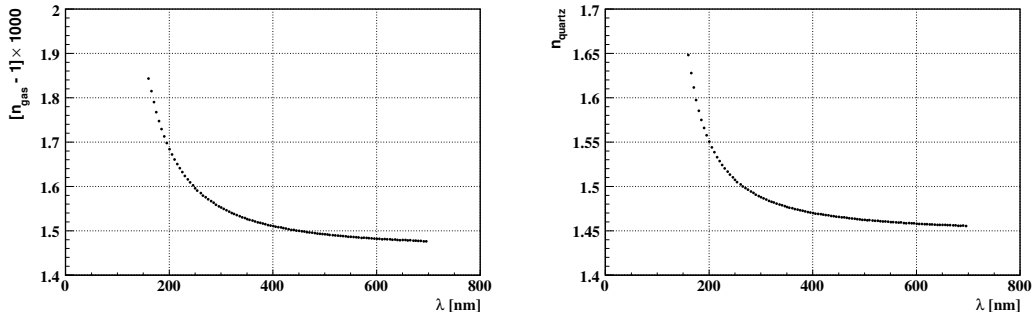


Figure 3. Refractive index of C_4F_{10} (left) and quartz (right) as a function of the wavelength.

The average number of photons emitted per unit of radiator length (L) in the wavelength range $[\lambda_1, \lambda_2]$ is approximately given by the formula [?]:

$$\frac{dN}{dx[\text{nm}]} = 2\pi\alpha \int_{\lambda_2}^{\lambda_1} \sin^2 \theta_C \frac{d\lambda}{\lambda^2} = 2\pi\alpha \int_{\lambda_2}^{\lambda_1} \left[1 - \left(\frac{1}{\beta n} \right)^2 \right] \frac{d\lambda}{\lambda^2}. \quad (8)$$

Assuming a C_4F_{10} (quartz) average refractive index of 1.00150 (1.47), which gives an average emission angle of 3.1° (46.8°), a relativistic particle crossing a tube along its axis ($\beta \approx 1$) at $P = 1.1$ bar and $T = 293.15^\circ$ kelvin emits about 990 (140) photons in the gas (quartz) in the wavelength range [160, 700] nm. Therefore, density and thickness of the PMT window are such that Cerenkov photons from the window are not negligible compared to those from the gas.

2.2 Light propagation and detection

2.2 Light propagation and detection

After being emitted in C_4F_{10} with a typical angle of 3° , photons are reflected by the inner walls of the tube with a certain efficiency (reflectivity). A typical aluminum surface reflectivity as a function of the photon wavelength can be found in [?]. This curve has been rescaled to match a bench measurement performed with red light. Depending on the position where they are generated, multiple reflections might occur before they actually reach the read-out photo-multipliers (see Figure 4).

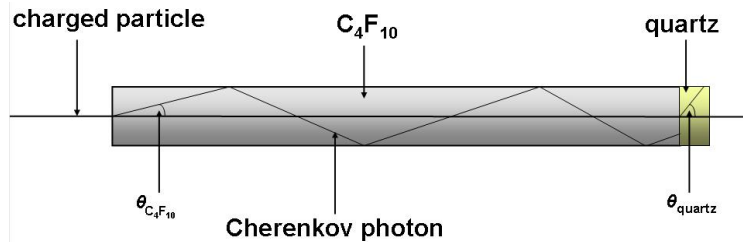


Figure 4. Light propagation inside a tube.

The average number of light reflections inside the tube is 2.8. Photons which are not absorbed by the gas reach the end of the tube and are converted by the PMTs into photo-electrons. The conversion efficiency (quantum efficiency) is wavelength dependent and is provided by the manufacturer (Hamamatsu) [?]. Tube reflectivity and quantum efficiency in the wavelength range accepted by the PMTs [160 nm, 700 nm] are shown in Figure 5 (numerical values are reported in Appendix A).

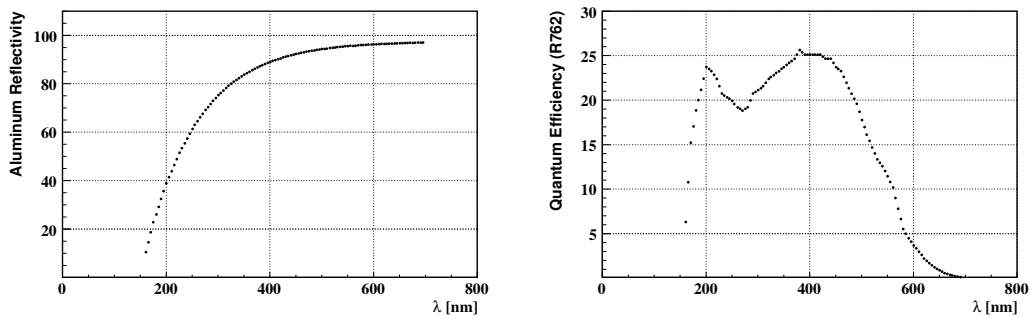


Figure 5. Aluminum tube reflectivity (left) and PMT quantum efficiency (right) as a function of photon wavelength.

Note that the dependence of reflectivity on photon polarization is not simulated. The absorption length of C_4F_{10} is assumed to be similar to that of Isobutane [?] (numerical values are reported in Appendix A). The effect of absorption in the quartz is contained in the quantum efficiency.

3 Response to a single particle

3 Response to a single particle

The geometry of LUCID is such that a particle originating from the IP (a primary particle) produces more light than a particle coming from any other direction (a secondary particle). The response of LUCID is simulated for particles originating from the IP and traveling either along the tube axis (on-axis) or a random direction (off-axis).

3.1 Signal from on-axis pions

A charged particle entering the tube and traveling along its axis emits Cerenkov photons in the gas and in the PMT quartz window. The number of photo-electrons read-out by the PMTs when 180 GeV charged pions travel along a tube axis is shown in Figure 6 (the signals in all 32 tubes are displayed).

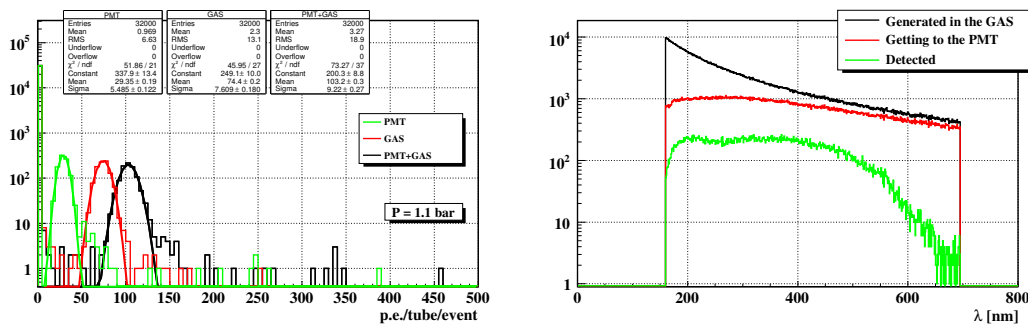


Figure 6. Distribution of photo-electrons detected by LUCID (left) and photon wavelength distribution (right), in 1000 events of single 180 GeV charged pions with $\theta = 0.00689$ and $\phi = 0$ (see text for details).

The red (green) histogram in the left plot of Figure 6 represents Cerenkov light emitted in the gas (quartz) and detected by the PMT. A total signal of 105 photo-electrons (black histogram) is produced by a particle traveling along a tube axis (75 from the gas and 30 from the PMT). The peak at zero is due to the fact that only one tube per event is crossed by a particle. Solid lines are the results of Gaussian fits. The value of the width is due to two contributions: the Poissonian fluctuation of Cerenkov emission and the binomial fluctuation of photo-electron conversion inside the PMT.

The wavelength spectrum of Cerenkov light at different stages inside a LUCID tube is shown in the right plot of Figure 6. The wavelength of generated photons (black line) has approximately a $1/\lambda^2$ shape. Generated photons traverse the gas and are reflected by the aluminum tube walls until they reach the quartz window (red line): the suppression at low λ is due to the absorption inside the gas and to the aluminum reflectivity. The effect of quantum efficiency is visible in the spectrum of detected photons (green line), which is strongly suppressed above 600 nm.

3.2 Signal from off-axis pions

3.2 Signal from off-axis pions

In a more realistic scenario, particles originating from pp collisions travel along directions different from the tube axis. In this section, the response of LUCID to particles traveling along random directions (off-axis) is studied.

When a primary particle crosses the detector tube walls, secondary particles are produced by interaction with the material. Secondary particles might cross the Cerenkov radiators (gas and quartz) and release light which will be added to the signal of the original primary particle. The trajectory of a secondary particle is typically transverse with respect to the axis of the Cerenkov tube, thus light emission is smaller compared to a primary particle (see Figure 7).

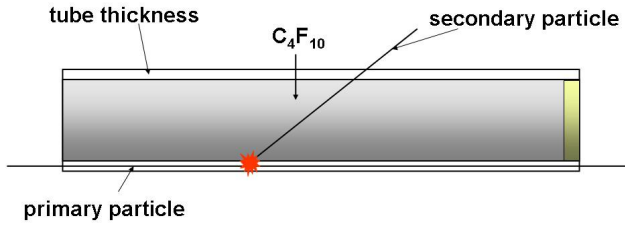


Figure 7. Path of a secondary particle produced by the interaction of a off-axis primary particle with the tube wall.

Off-axis primary particles are simulated by shooting 180 GeV pions from the IP with a flat polar angle between 4 and 10 mrad and a flat azimuthal angle between 0 and 2π . The resulting photo-electron spectrum is shown in Figure 8, with and without secondary interactions inside LUCID.

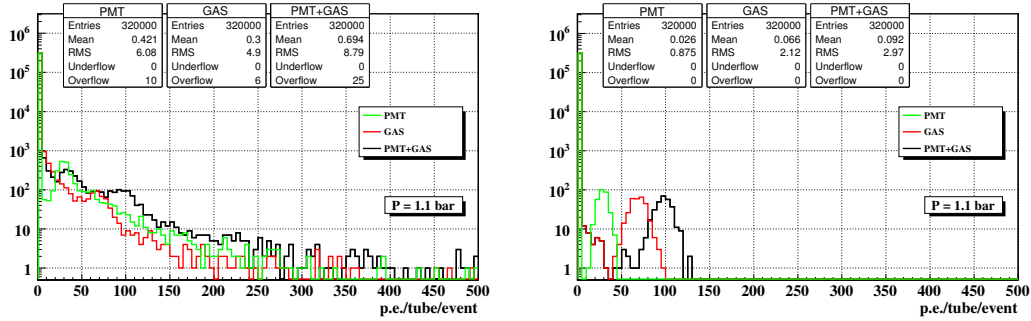


Figure 8. Left plot shows photo-electrons detected by LUCID in 10000 events of single 180 GeV pions shot from the IP with a random direction ($0.004 < \theta < 0.01$ and $0 < \phi < 2\pi$). Right plot shows the effect of neglecting secondary interactions inside the detector material (see text for details).

3.3 Signal from off-axis photons

The left plot in Figure 8 shows two peaks. The peak at about 105 photo-electrons is due to on-axis primary particles crossing both Cerenkov radiators (gas and quartz). The peak at 30 photo-electrons originates from secondary particles crossing only the quartz. Compared to Figure 6, a continuous background is created by secondary particles. Even though tube walls are thin (≈ 1 mm), the effective thickness traversed by off-axis primaries is large (≈ 1500 mm), which results in a large probability for secondary interactions. The effect is only partially suppressed by the smaller path length of secondaries inside the Cerenkov radiator.

When the effect of secondary particles is neglected (right plot in Figure 8), the photo-electron spectrum of off-axis primaries is similar to that of on-axis primaries (left plot in Figure 6). This is due to the fact that LUCID tubes are so “far” from the IP (about 17 m) that off-axis primary particles are almost parallel to the tube axis, therefore the path inside the radiator of off-axis and on-axis primaries are similar.

3.3 Signal from off-axis photons

Neutral particles do not emit directly Cerenkov photons when crossing the LUCID detector. Still, the effect of neutral particles might be not negligible due to the production of charged particles in secondary interactions with the LUCID tube walls. The spectrum of photo-electrons detected by LUCID due to 100 GeV photons is shown in Figure 9.

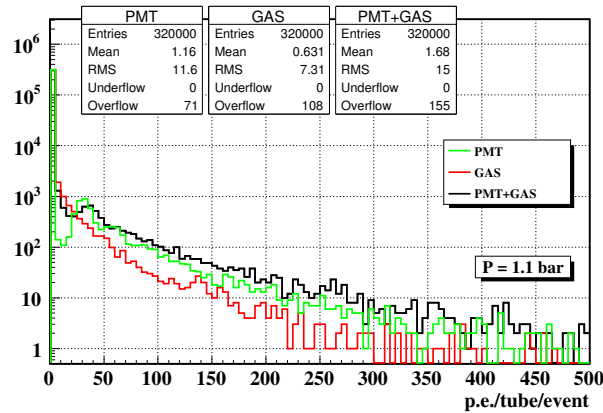


Figure 9. Photo-electrons detected by LUCID in 10000 events of single 100 GeV photons shot from the IP with a random direction ($0.004 < \theta < 0.01$ and $0 < \phi < 2\pi$).

The peak at 30 photo-electrons is due to secondary particles crossing only the PMT quartz window. Compared to Figure 8, the peak at about 105 photo-electrons is not visible due to the fact that secondary particles typically do not travel along the tube axis.

4 Response to pp collisions

4 Response to pp collisions

Primary pp collisions at 14 TeV center of mass energy are simulated according to the production cross sections and decay branching ratios provided by PHOJET (version 1.12.1.35) [?]. Particles are fed through a GEANT3-GCALOR [?] simulation of the ATLAS detector in order to describe the interaction of primary particles with the detector material up to LUCID mother volume (a volume containing the LUCID detector). All primary and secondary particles hitting the LUCID mother volume are finally used as input for the last simulation step in which the LUCID performance is evaluated with the GEANT4 [?] detector simulation illustrated in Section 2. Background originating from beam halo and beam-gas interactions inside the beam pipe is not simulated. The main features of tracks entering the LUCID mother volume are compared to those of tracks detected by LUCID.

4.1 Event generator

Several packages are available for the simulation of the physics processes occurring in pp collisions. The difference among them reflects the systematic uncertainty in the models which are used to describe the interaction of protons.

The total pp cross-section can be divided into elastic and inelastic components, and the inelastic component can be further divided into: non-diffractive, single diffractive and double diffractive components [?]. The total cross-section (σ_{tot}) can then be written as:

$$\sigma_{tot} = \sigma_{el} + \sigma_{sd} + \sigma_{dd} + \sigma_{nd}$$

where these cross-sections are elastic (σ_{el}), single diffractive (σ_{sd}), double diffractive (σ_{dd}) and non-diffractive (σ_{nd}), respectively. The production cross section of the different inelastic processes predicted by PYTHIA [?] and PHOJET [?] at the center-of-mass energy of 14 TeV are reported in Table 2 (cross sections at 10 TeV are expected to be 10% lower [?]).

Type of pp collision	σ [mb] in PYTHIA	σ [mb] in PHOJET
Non-diffractive	55	69
Single-diffractive	14	11
Double-diffractive	10	4
Total inelastic	79	84

Table 2. Cross section of inelastic processes in pp collisions at 14 TeV predicted by PYTHIA and PHOJET. The table and the list of generator settings can be found in [?].

4.1 Event generator

As far as LUCID is concerned, elastic interactions are neglected because protons scatter at small angles and interact further downstream. The pseudo-rapidity of all charged particles produced in single-, double- and non-diffractive processes predicted by PYTHIA and PHOJET are shown in Figure 10.

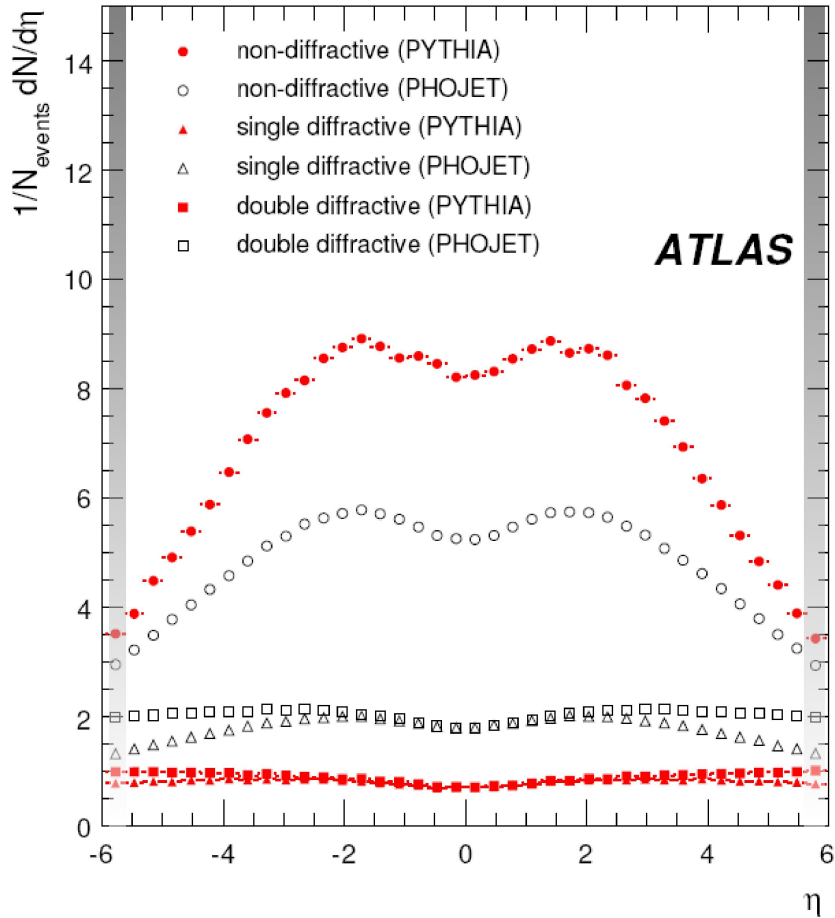


Figure 10. Pseudo-rapidity of stable charged particles in different types of inelastic pp collisions as predicted by PHOJET (open symbols) and PYTHIA (closed symbols) [?]. The acceptance region of LUCID is highlighted ($5.6 < \eta < 6.2$).

Although the predictions on the total cross section of PYTHIA and PHOJET are close, the two generators forecasts a different particle multiplicity and a different sharing of event types especially in the pseudo-rapidity range in which LUCID operates ($5.6 < \eta < 6.2$).

There is no ground at present to consider one generator more reliable than the other. The study presented in this note is done with about 9159 events of single pp interactions generated with PHOJET 1.12.1.35 [?] in the full pseudo-rapidity range.

4.2 Track propagation inside ATLAS

4.2 Track propagation inside ATLAS

Generated particles are fed through a GEANT3-GCALOR [?] simulation of the ATLAS detector including all sub-systems (magnets, trackers, calorimeters etc.), with the exception of LUCID. The generator settings and detector geometry used in a previous study of radiation background [?] are chosen here due to the particular attention given to low energetic processes, such as electromagnetic showers, which are essential for the study of radiation background.

Being located close to the beam pipe inside the forward muon shielding, LUCID is exposed to a large flux of secondary particles. In fact, primary particles produced by inelastic pp collisions interact with the material of the experiment producing secondary particles that may reach LUCID from any direction.

The energy threshold for particle detection in LUCID is such that the effect of secondary particles might be not negligible (only 10 MeV for electrons).

The original idea behind the LUCID design was to build a detector capable of distinguishing between primary and secondary particles. Due to the projective geometry of LUCID, primary particles travel typically longer paths inside a tube compared to secondary particles (see Figure 11). Primary particles are therefore expected to emit more Cerenkov light than secondaries.

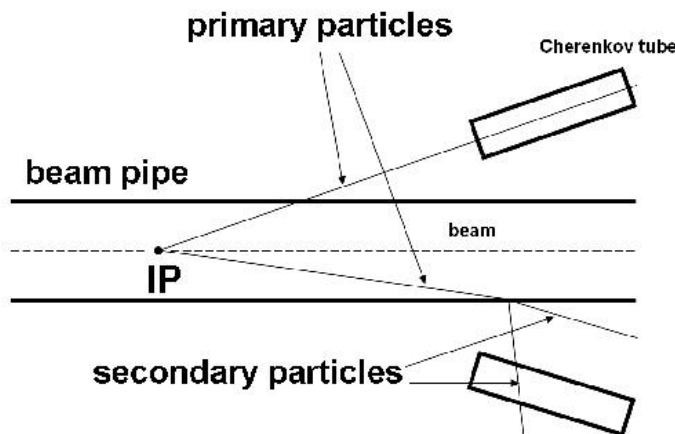


Figure 11. Schematic view of primary and secondary particle path inside LUCID. Here the secondaries are due to the interaction between the primary and the beam pipe.

4.3 The LUCID volume

The LUCID volume is defined around the region where the LUCID tubes are actually located. It has similar dimensions to the external vessel in which the Cerenkov tubes are contained. The position and the four-vectors (energy and momentum) of all particles hitting the surface delimiting this volume is recorded, together with the

4.3 The LUCID volume

information of the type and the origin (primary or secondary) of the particle. The coordinates of the impact points for a subset of events is shown in Figure 12. The volume is defined in such a way that it contains LUCID and it does not clash with the neighborhood ATLAS detector subsystems.

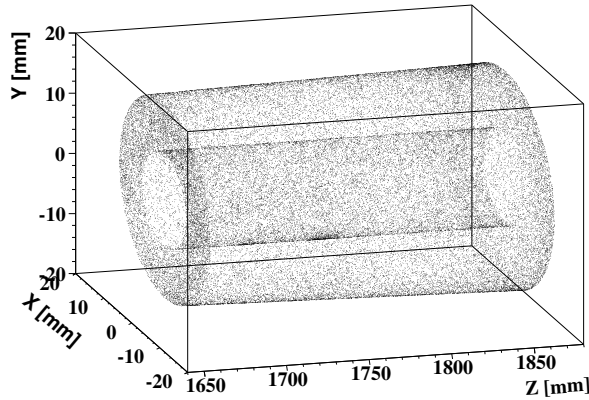


Figure 12. The LUCID volume (the z coordinate is along the beam axis).

One can compare the number of primary and secondary particles reaching the LUCID volume (see Figure 13).

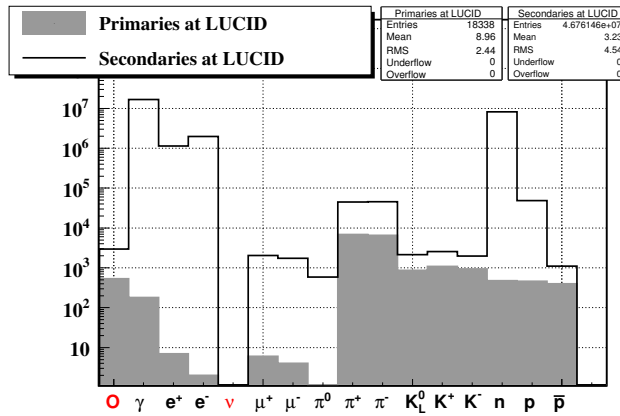


Figure 13. Distribution of primary particles at the IP (dashed line), primary (filled grey) and secondary particles (solid line) at the LUCID volume. The first bin is the overflow.

Most primary particles (filled grey) are pions. Photons from $\pi^0 \rightarrow \gamma\gamma$ prompt decays are also labeled as primary particles, but most of them are absorbed before reaching LUCID. Secondary particles reaching the LUCID volume (solid line) are mostly electrons and photons from electromagnetic showers, while neutrons are due to back-scattering from the material placed downstream of LUCID.

4.4 Definition of the particle direction

4.4 Definition of the particle direction

The number of photo-electrons produced by a charged particle crossing a LUCID tube is proportional to the path length inside the Cerenkov radiators (gas and quartz). Particles coming from the interaction point and hitting the LUCID volume on the front side that face the interaction point are expected to travel the longer path inside the tubes and to give a larger contribution of photo-electrons.

In order to study the correlation between the original direction of the particles and the size of the signal inside LUCID, a direction is associated to each particle. The coordinate of the impact point (x, y, z) and the momentum (p_x, p_y, p_z) of primary and secondary particles are used to define a direction for each particle. In this analysis, particles are divided in three classes: front, side and back.

If $z \times p_z < 0$, the particle is defined as “back”. If the particle is not “back” and if $|z| > 16601$ mm, the particle is defined as “side”. The remaining particles are defined as “front”.

The z coordinate (the one along the beam axis) of the impact point of all particles on LUCID volume is plotted in Figure 14.

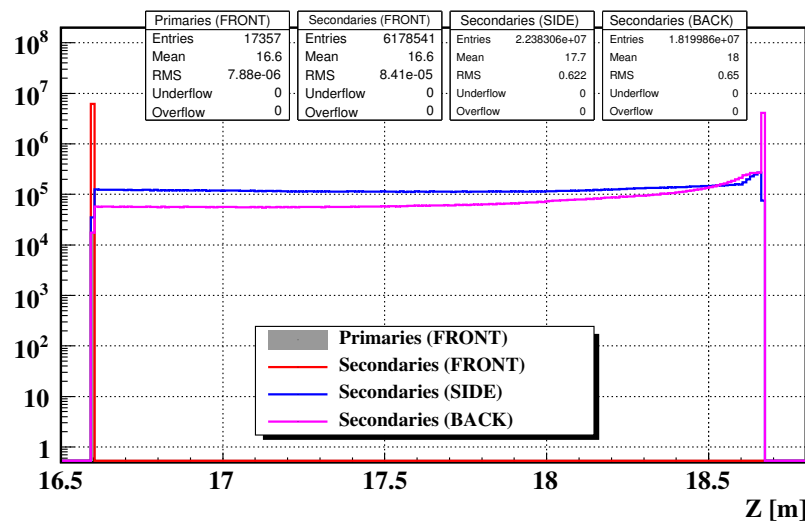


Figure 14. Distance from the IP (along the beam axis) of the impact point on LUCID. The results are shown for the three classes of particles defined in the text (“front”, “side” and “back”).

Of the particles hitting LUCID from the front, only 0.3% are primaries. Most of the particles hitting the LUCID volume are, however, particles coming from the side or the back (85%).

4.5 Track propagation inside LUCID

4.5 Track propagation inside LUCID

The impact point, the arrival time and the energy at the LUCID volume is used as seed for the track propagation inside the volume with the stand-alone GEANT4 simulation presented in Section 2. One important feature of the analysis presented in this chapter is the traceability of the particles. If a particle generates secondaries inside the LUCID detector material, the release of light due to secondaries is associated to the original track.

4.6 Photo-electron spectrum

The response of LUCID to inelastic pp collisions in terms of photo-electrons per tube per event is shown in Figure 15.

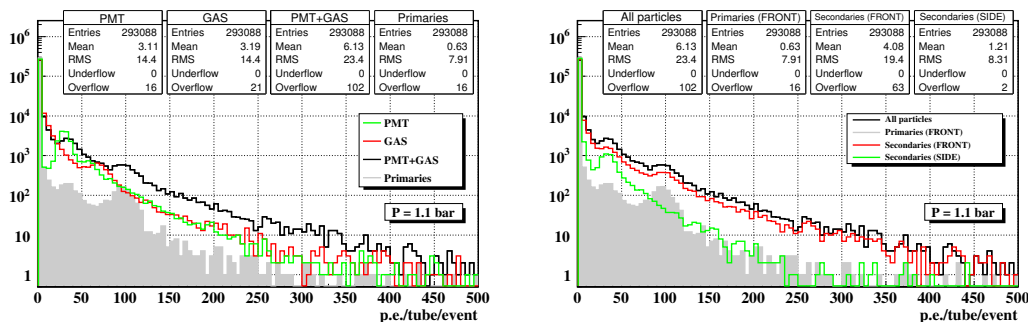


Figure 15. Spectrum of photo-electrons read-out by LUCID in 9159 inelastic pp collisions. Contributions from different radiators (left) and particle directions (right) are shown.

On the left plot, peaks at the expected positions for production of photo-electrons in the gas (75) and quartz (30) are visible, together with their sum at 105 photo-electrons. Together with the total number of photo-electrons, the right plots show three contributions: primary particles (grey area), “front” secondaries (red line) and “side” secondaries (green line).

The spectrum of primary particles is similar to the one shown in Figure 8, which was obtained shooting high energy pions from the IP with a flat polar angle distribution. Compared to those coming from the “front”, “side” secondaries travel a smaller path into the tube, thus releasing less Cerenkov light.

4.7 Hit definition

The average number of photo-electrons produced by an on-axis primary particle is about 105 (Figure 6). The largest fraction of secondaries releases light only in the PMT window (30 photo-electrons). A cut-off threshold of 50 photo-electrons allows us to keep the entire signal of primary particles, while suppressing large fraction of secondaries which are not directly correlated with primary particle.

4.8 Time of flight

Such threshold allows one to remove also light detection related effects (dark current and thermo-ionic emission) which are at level of few photo-electrons. The main features of tracks entering the LUCID volume (arrival time, impact angle and energy) are compared to those of tracks detected by LUCID when a signal of at least 50 photo-electrons is registered.

4.8 Time of flight

Particles produced by protons colliding at 14 TeV center of mass energy travel approximately at the speed of light inside the ATLAS detector. The time needed by primary particles to cover the distance from the interaction point to the front side of LUCID in a straight line is about 56 ns. For geometrical reasons, the time of arrival of secondaries is expected to be longer since they travel longer paths before hitting the LUCID volume. This is especially true for secondary particles hitting the side or the back of the volume. The time of flight of particles reaching the LUCID volume is shown in Figure 16.

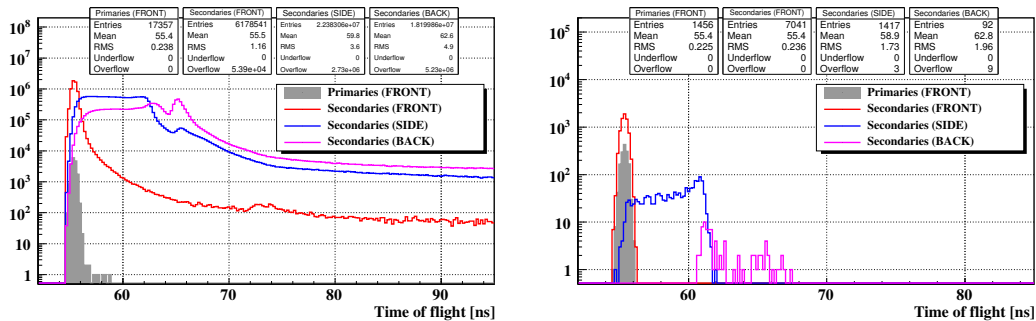


Figure 16. The left plot shows the time of arrival of all particles to the LUCID volume. The right plot is obtained for particles detected by LUCID (> 50 p.e.).

The left plot shows that detected “front” secondaries which are in time with primaries (within 2 ns) are about a factor 5 more than primaries. Secondaries from the side are about 20% more than primaries and are spread over a larger range of time due to the shape of the LUCID volume. Detected secondaries from the back are negligible. Detected “side” and “back” secondaries have a peak at about 61 ns, which is the time needed to reach the position of the PMT.

4.9 Angle with the beam

Primary and secondary particles detected by LUCID hit almost simultaneously the front face of the LUCID volume. However, secondary particles, being the product of scattering of primary particles through different materials, are expected to travel along different directions with respect to primaries. The angle between the beam axis and the trajectory of primary and secondary particles is shown in Figure 17.

4.10 Energy

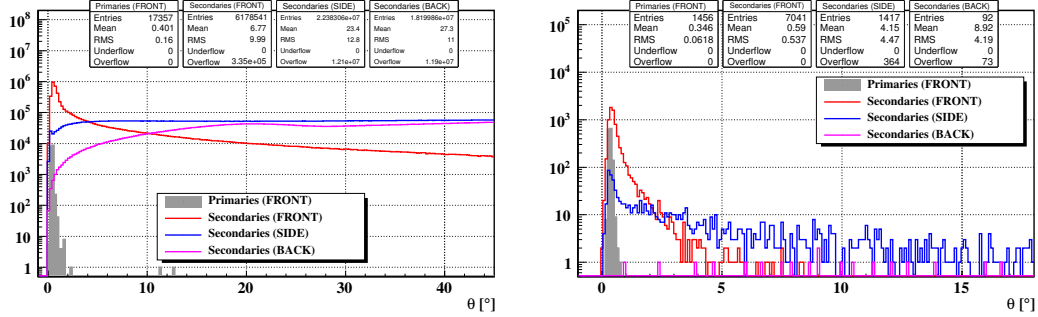


Figure 17. The left plot shows the angle with the beam axis of particles crossing the LUCID volume. The right plot is obtained for particles detected by LUCID (> 50 p.e.).

A comparison between the left and right plots shows that “front” and “side” secondaries with a angle larger than 2° are both strongly suppressed when required to give a signal in LUCID, due to the pointing nature of particle detection in LUCID. The angle of detected primary particles is less than 1° and has an average of 0.35° . The peaks of “front” and “side” secondaries are at the same position of primaries but distributions are broader (with an average of 0.6° and 4.1°). Secondaries from the “back” have larger angles.

4.10 Energy

Primary particle are mostly pions, while secondary particles are mostly photons and electrons. As a reminder, Cerenkov light associated to a γ is that emitted by secondary charged tracks coming from γ interactions (ex: $\gamma \rightarrow e^+e^-$). The energy distribution of primary and secondary pions are shown in Figure 18.

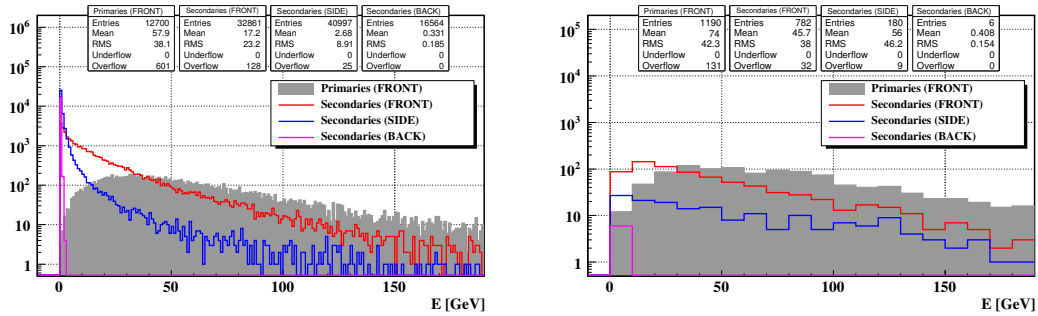


Figure 18. Energy distribution of pions crossing the LUCID volume (left) and detected by LUCID requiring more than 50 photo-electrons (right).

The requirement of being detected by LUCID suppresses the soft particles. The average energy of a detected primary pion is 74 GeV, which is larger than that of secondary pions from the front (46 GeV) and from the side (56 GeV). Pions from

5 Study of luminosity monitoring algorithms

the back have much smaller energy (0.4 GeV). The energy distribution of primary and secondary photons and electrons are shown in Figure 19.

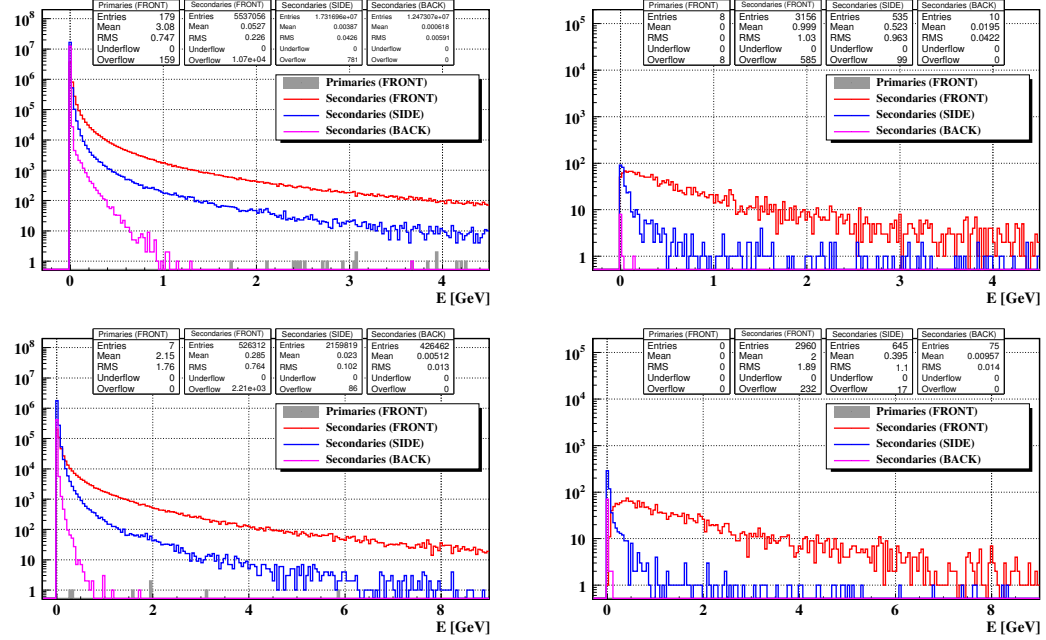


Figure 19. Energy distribution of photons (top) and electrons (bottom) crossing the LUCID volume (left) and detected by LUCID requiring more than 50 photo-electrons (right).

Primary photons and electrons on the LUCID volume are negligible. As for pions, the requirement of being detected by LUCID suppresses the soft part of the energy spectrum. The average energy of a detected “front” secondary photon (electron) is 1 GeV (2 GeV). Most secondary particles from the “back” have an energy below the Cerenkov threshold.

5 Study of luminosity monitoring algorithms

This section is dedicated to the study of the LUCID performance as a luminosity monitoring system. The Monte Carlo simulation of the full ATLAS detector described in Section 4 is used to simulate the calibration and the measurement event samples. The calibration sample consists of 9159 single pp interaction events. The measurement samples are built by overlapping single pp interactions events according to Poissonian distributions. The average number of pp interactions per event (μ_{meas}) is extracted from the measurement samples at high luminosity with several methods and the result is compared with the true value (μ_{true}).

5.1 Definition of the type of detected pp interaction

5.1 Definition of the type of detected pp interaction

LUCID consists of two modules placed symmetrically around the ATLAS interaction point. Two criteria to detect a pp collision can be defined: single side mode and coincidence mode. In single side mode, a pp interaction is detected if there is at least 1 hit in *one module*. In coincidence mode, a pp interaction is detected if there is at least 1 hit in *both modules* (see Figure 20).

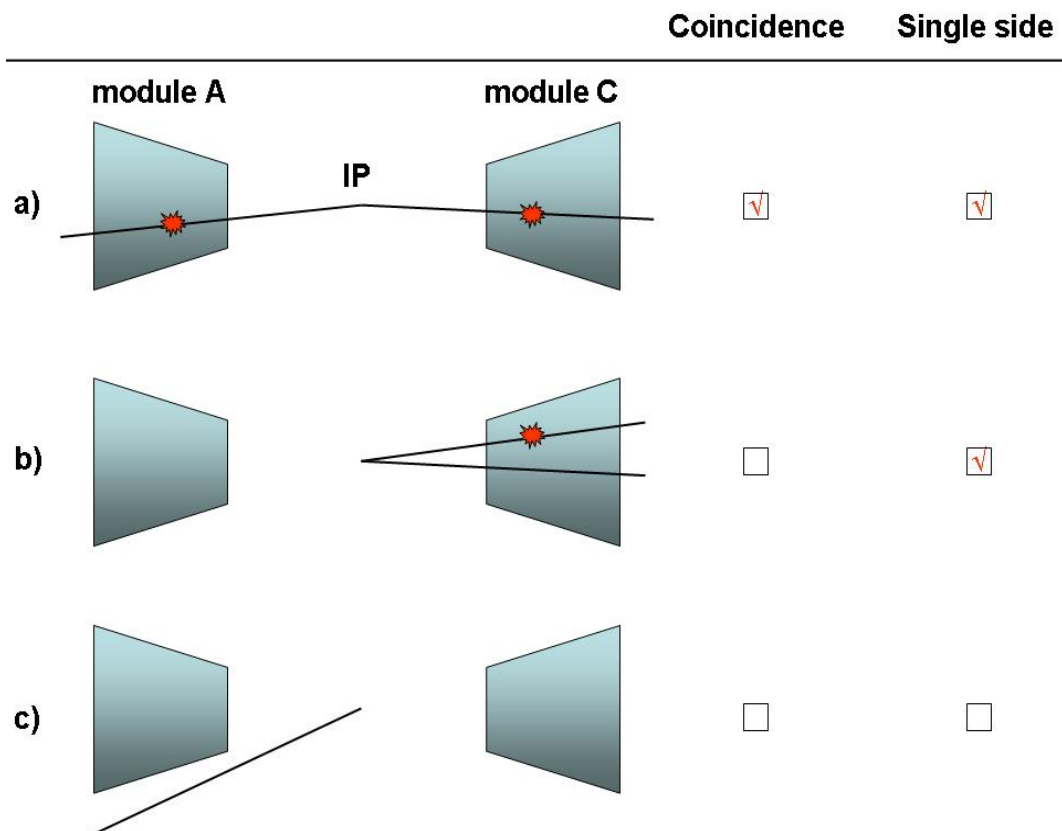


Figure 20. Principle of detection in single side and coincidence modes.

In a) each module detects a particle. This interaction is detected both in single side mode and in coincidence mode. In b) two particles traverse the same module, one of them giving a hit. This interaction is detected in single side mode only. In c) no particle traverses any modules and no interaction is detected.

The advantage of requiring a coincidence is that background produced by beam interactions with residual gas inside the beam pipe or by the beam-halo from the LHC collimators is reduced. Such background is uncorrelated with the ATLAS interaction point and is typically detected in one module only.

5.2 Detection efficiency and hit distribution

5.2 Detection efficiency and hit distribution

The detection efficiency and the average number of hits per pp collision are extracted from the calibration sample for different criteria used to define a hit. The detection efficiency is $(55.8 \pm 0.05)\%$ in single side mode and $(13.5 \pm 0.4)\%$ in coincidence mode. The average number of hits per pp collision is 1.21 ± 0.02 in single side mode, and 0.49 ± 0.01 in coincidence mode. The smaller value in coincidence mode is due to the smaller probability of having a hit simultaneously in both modules. Hit multiplicity and tube hit probability are shown in Figure 21.

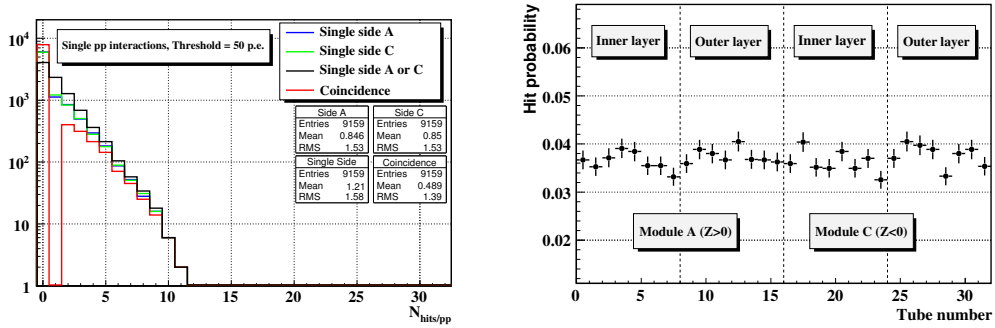


Figure 21. Number of LUCID hits with a 50 p.e. threshold (left) and hit probability (right) per pp interaction.

The probability to have a hit in a tube is approximately the same for all tubes. For tube 0, the hit probability is $(3.7 \pm 0.2)\%$. The efficiency to detect a pp interaction in single side mode (ε^{Sing}), coincidence mode (ε^{Coin}), in side A (ε^A) and side C (ε^C) and the corresponding average number of hits per pp interaction in the full detector are reported in Table 3.

Trigger	Efficiency [%]	$N_{hits/pp}$	N_{hits/pp^*}
Single Side	$\varepsilon^{Sing} = 55.8 \pm 0.5$	1.21 ± 0.02	2.16 ± 0.02
Coincidence	$\varepsilon^{Coin} = 13.5 \pm 0.4$	0.49 ± 0.01	3.62 ± 0.05
Side A	$\varepsilon^A = 34.3 \pm 0.5$	0.85 ± 0.02	2.47 ± 0.03
Side C	$\varepsilon^C = 35.0 \pm 0.5$	0.85 ± 0.02	2.43 ± 0.03

Table 3. Efficiency and number of hits per pp interaction with a 50 p.e. threshold for different trigger configurations. The symbol pp^* indicates that the average is performed on detected interactions only.

Terms ε^A and ε^C are the probability of detecting a pp interaction on one side, regardless of what happens in the other side (they include coincidences). By definition, N_{hits/pp^*} is larger than 1 (2) in single side (coincidence) mode.

5.3 Simulation of high luminosity events

5.3 Simulation of high luminosity events

The measurement samples are built by overlapping single pp interaction events according to Poissonian distributions ($\mu = 0.01, 0.05, 0.1, 1, 2, 5, 10, 15, 20, 25$). Single pp interaction events are selected randomly from the calibration sample and are used twice in each measurement sample, therefore uncertainties are increased by a factor of $\sqrt{2}$. When μ goes from 1 to 25, the photo-electron distribution becomes more flat and the average increases from 6.1 to 144 (see Figure 22).

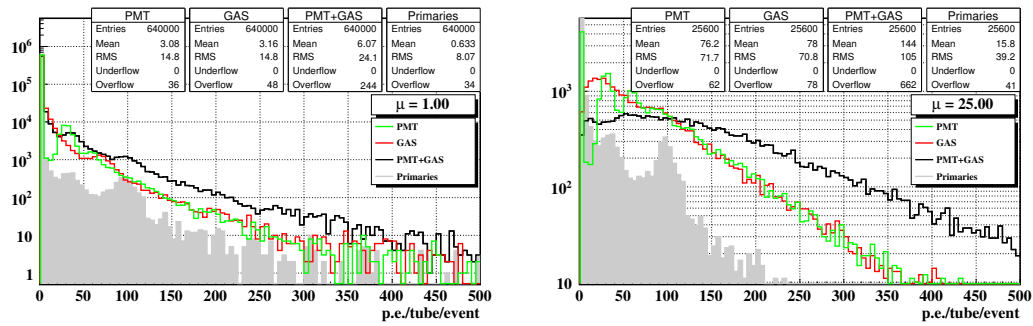


Figure 22. Photo-electron spectra when $\mu = 1$ (left) and $\mu = 25$ (right).

Due to an increased track multiplicity, the signal of primary particles is hidden by the combinatorial background of secondaries crossing the tubes at large angles and giving small signals. The effect of several secondaries with small signals adding up to give a large signal is called the **migration effect**.

For $\mu = 1$ and a 50 p.e. threshold, the average number of hits is 1.22 ± 0.02 in single side mode and 0.73 ± 0.02 in coincidence mode (see Figure 23).

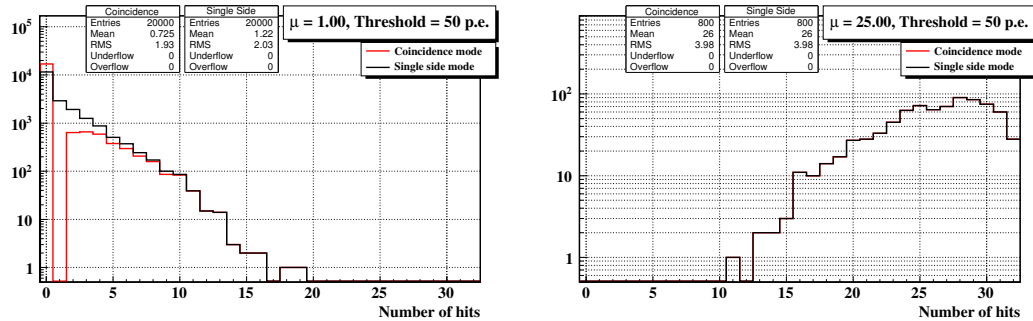


Figure 23. Hit distributions with a 50 p.e. threshold for $\mu = 1$ (left) and $\mu = 25$ (right).

Note that the hit distributions in single side mode and in coincidence mode becomes identical when $\mu = 25$ because all detected events have at least 1 hit in both modules (the average number of hits per event is 26.0 ± 0.2).

5.4 Counting methods

5.4 Counting methods

The average number of pp interactions per event (μ_{meas}) is extracted from the high luminosity samples with several methods and the results are compared with the true value (μ_{true}).

5.4.1 Zero counting

The basic idea of the zero counting method is to extract μ from the frequency of empty events $P_{0/BX}$ (those without pp collisions). For an ideal detector (100% efficient) in single side mode, the following relation holds (see Equation 13 in Appendix B):

$$\mu = -\log(P_{0/BX}).$$

The definition of an empty event depends on the definition of a detected pp interaction. In single side mode, empty events have 0 hits in both modules. In coincidence mode, empty events have 0 hits in at least one module.

The zero counting method has the advantage of simplicity since it relies on counting events rather than hits. A drawback of this method is that the rate of empty events decreases by increasing luminosity, especially for detectors with a large detection efficiency. At design luminosity ($L = 10^{34} \text{ cm}^{-2}\text{s}^{-1}$), the average number of pp interactions per event is 25, which implies a rate of empty events of $e^{-25} \times 40 \text{ MHz} = 5.6 \times 10^{-4} \text{ Hz}$ (40 MHz is the crossing rate). In case of LUCID, a possible solution is to reduce the detection efficiency by reducing the number of tubes.

5.4.2 Hit counting

The basic idea of a hit counting method is to extract μ from the number of hits registered by LUCID. Under the assumption that the number of particles per event scales linearly with the number of pp collisions in single side mode, the following relation holds:

$$\mu = \frac{N_{part/BX}}{N_{part/pp}}$$

where $N_{part/BX}$ is the number of particles per event and $N_{part/pp}$ is the number of particles per pp interaction. Under certain assumptions, the number of particles can be turned into hits registered in LUCID using the prescription described in Appendix D. The advantage of this method compared to the zero counting method is that it can be used at any luminosity.

5.5 Linear extrapolation model

5.5 Linear extrapolation model

The response of LUCID can be parametrized with a linear function of μ :

$$R(\mu) = k_{LUCID} \times \mu$$

The calibration constant (k_{LUCID}) can be extracted from a low luminosity run ($\mu << 1$) in which the probability of having overlapping pp interactions is negligible. In the following, the calibration is done at $\mu = 0.01$ ($k_{LUCID} = R(0.01)/0.01$).

Zero counting Equation 13 in Appendix B shows that μ can be extracted from the fraction of empty events in single side mode ($P_{0/BX}$) by taking:

$$\mu = \frac{-\log(P_{0/BX})}{k_{LUCID}}$$

where k_{LUCID} is the detection efficiency. In coincidence mode, this is an approximation (see Equation 23 in Appendix B). The measurements of μ with the linear model in zero counting² are plotted against the true value in Figure 24.

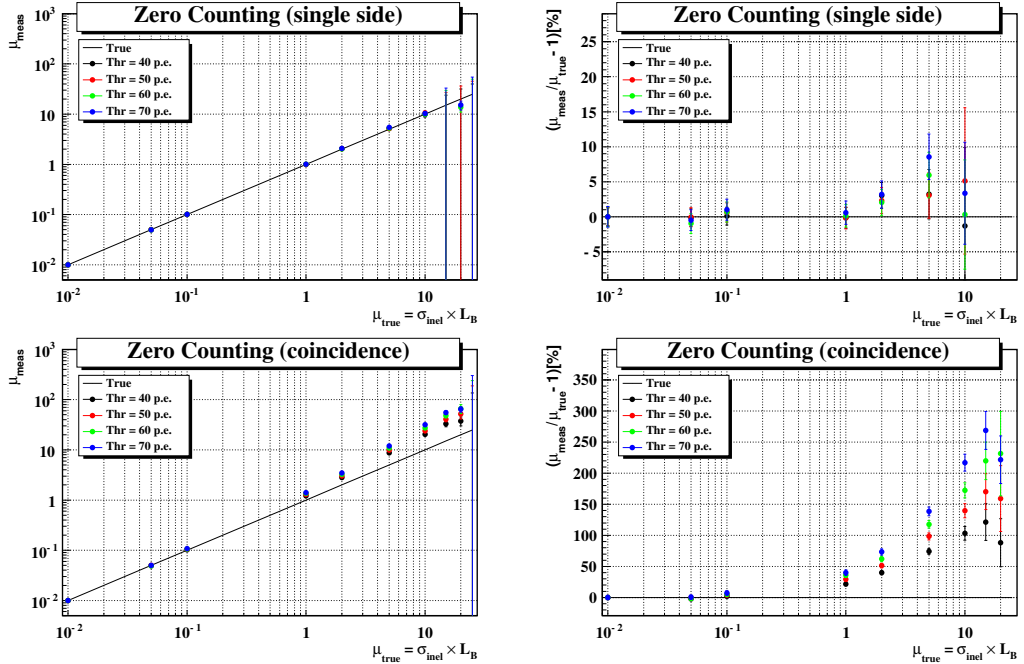


Figure 24. Left: average number of pp interactions per event measured with the linear model (μ_{meas}) in zero counting single side (top) and coincidence mode (bottom) as a function of the true value (μ_{true}) for different thresholds. Right: deviation from the true value.

²The uncertainty on μ_{meas} is statistical only and the uncertainty on k_{LUCID} is neglected.

5.5 Linear extrapolation model

In single side mode with a 50 *p.e.* threshold, $k_{LUCID} = 0.553 \pm 0.007$. The difference between the measured and the true μ is within the uncertainty (2%) when $\mu < 2$. The detection efficiency increases at larger μ due to the migration effect (see Section 5.3), therefore the number of empty events is smaller than the prediction. The uncertainty is dominated by the lack of empty events for $\mu > 5$.

In coincidence mode with the same threshold, $k_{LUCID} = 0.133 \pm 0.004$ and the deviation is already 4% at $\mu = 0.1$ due to the use of an approximated formula. The deviation increases with the threshold due to an increased migration effect.

Hit counting In Section 5.4.2 it is assumed that μ can be extracted from the average number of hits per event in single side mode ($N_{hits/BX}$) by taking:

$$\mu = \frac{N_{hits/BX}}{k_{LUCID}}$$

where k_{LUCID} is the average number of hits per *pp* collision. In coincidence mode, this is an approximation (see Equation 43 in Appendix C). The measurements of μ with the linear model in hit counting³ are plotted against the true value in Figure 25.

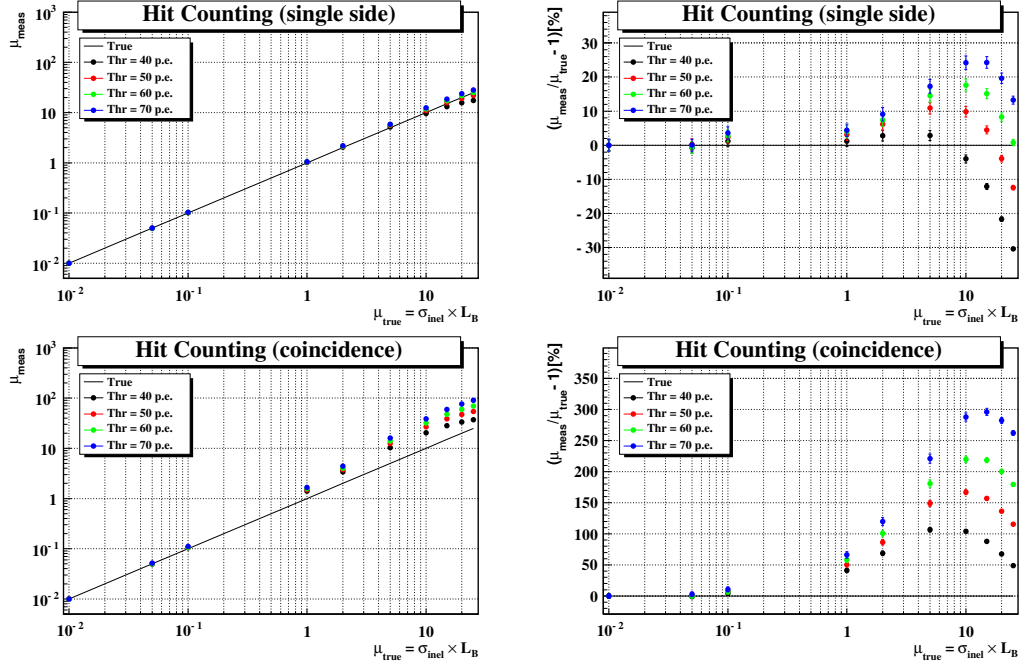


Figure 25. Left: average number of *pp* interactions per event measured with the linear model (μ_{meas}) in hit counting single side (top) and coincidence mode (bottom) as a function of the true value (μ_{true}) for different thresholds. Right: deviation from the true value.

³The uncertainty on μ_{meas} is statistical only and the uncertainty on k_{LUCID} is neglected.

5.6 Combinatorial model

In single side mode with a 50 *p.e.* threshold, $k_{LUCID} = 1.19 \pm 0.02$ and the difference between the measured and the true μ is within the uncertainty (2%) when $\mu < 1$. The deviation at larger μ is due to two effects: the migration and the saturation.

The **migration effect** is the simultaneous occurrence of several small signals in the same tube which add up and “migrate” above the threshold when μ is sufficiently large. Due to an increased number of hits, this effect leads to an overestimate of μ .

The **saturation effect** arises from counting hits instead of particles. The number of particles increases constantly with μ while the maximum number of hits is limited to 32 (the number of tubes). When μ is sufficiently large ($\mu > 5$), the large number of particles saturates the detector and lead to an underestimate of μ . Note that the deviation increases with the threshold due to an increased migration effect.

In coincidence mode with the same threshold, $k_{LUCID} = 0.482 \pm 0.015$ and the deviation from linearity is already 7% at $\mu = 0.1$. Compared to the single side mode, the deviation is larger due to the use of an approximated formula.

5.6 Combinatorial model

To reduce the uncertainty of the linear model, the response of LUCID for zero ($P_{0/BX}$) and hit counting ($N_{hits/BX}$) are analytically computed using the detection efficiency and the average number of hits per detected pp interaction obtained from the calibration sample. Calculations are reported in Appendix B and C.

Zero counting The average number of pp interactions per event is related to the fraction of empty events in single side mode ($P_{0/BX}$) and to the detection efficiency (ε^{Sing}) by Equation 13 of Appendix B:

$$\mu = -\frac{1}{\varepsilon^{Sing}} \log(P_{0/BX})$$

In coincidence mode, $P_{0/BX}(\mu)$ is given by Equation 23 of Appendix B:

$$P_{0/BX}(\mu) = f(\mu) = e^{-\mu\varepsilon^A} + e^{-\mu\varepsilon^C} - e^{-\mu(\varepsilon^A + \varepsilon^C - \varepsilon^{Coin})}$$

This equation cannot be inverted analytically, therefore the average number of pp interactions per event is obtained by numerical inversion with a 10^{-10} precision:

$$\mu = f^{-1}(P_{0/BX})$$

The uncertainty on μ is evaluated as the maximum variation of μ corresponding to a $\pm 1 \sigma$ variation of $P_{0/BX}$. The uncertainties on the efficiencies are neglected. The measurements of μ with the combinatorial model in zero counting are plotted against the true value in Figure 26.

5.6 Combinatorial model

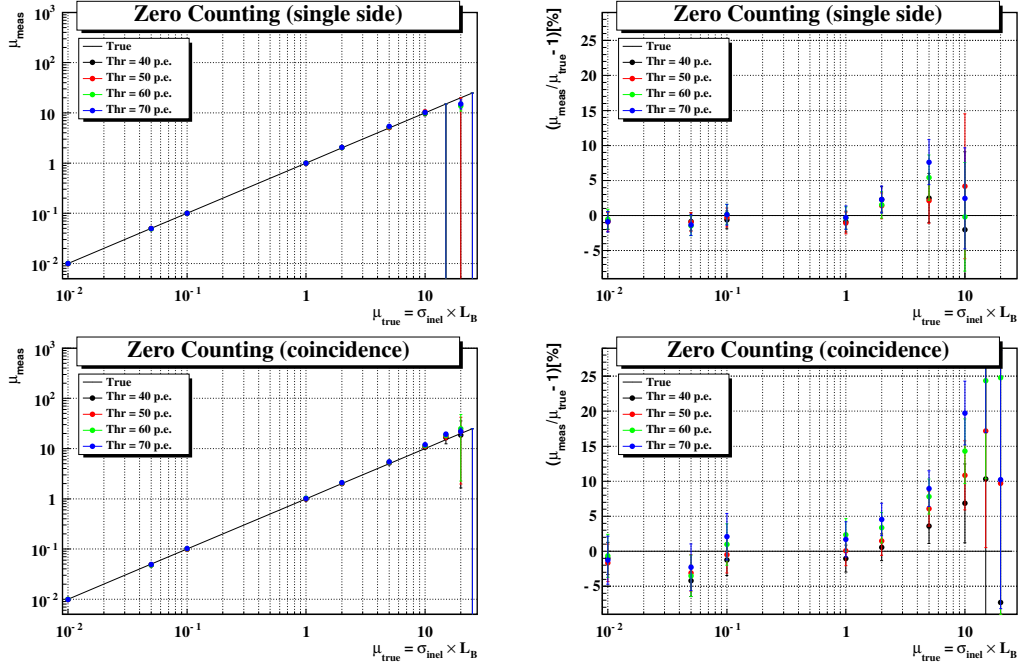


Figure 26. Left: average number of pp interactions per event measured with the combinatorial model (μ_{meas}) in zero counting single side (top) and coincidence mode (bottom) as a function of the true value (μ_{true}) for different thresholds. Right: deviation from the true value.

In single side with a 50 *p.e.* threshold, the agreement between the measured and the true number of pp interactions is within the uncertainty (2%) when $\mu < 2$. The detection efficiency increases at larger μ due to the migration effect (see Section 5.3), therefore the number of empty events is smaller than the prediction and μ is overestimated. The uncertainty is dominated by the lack of empty events for $\mu > 5$,

In coincidence mode with the same threshold, the agreement between the measured and the true number of pp interactions is within the uncertainty (3%) when $\mu < 2$. The deviation increases with the threshold due to an increased migration effect.

Note that the combinatorial model has the same accuracy of the linear model in single side mode. In coincidence mode, the prediction of the combinatorial model is as accurate as in single side mode, while the linear model fails already at $\mu = 0.1$. The accuracy of the combinatorial model for $\mu < 2$ is an upper limit and can be improved by increasing the size of the calibration sample.

5.6 Combinatorial model

Hit counting The average number of pp interactions per event in single side mode can be written as:

$$\mu = \frac{N_{par/BX}}{N_{part/pp}}$$

where $N_{part/BX}$ is the average number of particles per event and $N_{part/pp}$ is the average number of particles per pp interaction. The number of particles is related to the number of hits by Equation 46 in Appendix D, therefore one can write:

$$\mu = \frac{\log \left(1 - \frac{N_{hits/BX}}{N_{tubes}} \right)}{\log \left(1 - \frac{N_{hits/pp}}{N_{tubes}} \right)}$$

The number of tubes (N_{tubes}) is 32, while $N_{hits/pp}$ is reported in Table 3. Note that the hit counting method in single side mode is equivalent to a zero counting method at the level of the single tube, the result being the average on all tubes. Since the detection efficiency of the single tube is small enough, the method can be applied up to $\mu = 25$.

The average number of particles per event in coincidence mode is given by Equation 43 in Appendix C:

$$N_{part/BX} = \mu N_{part/pp}^{Coin} + \mu \left(N_{part/pp}^A - N_{part/pp}^{Coin} \right) \left(1 - e^{-\mu \varepsilon^C} \right) + \mu \left(N_{part/pp}^C - N_{part/pp}^{Coin} \right) \left(1 - e^{-\mu \varepsilon^A} \right) \quad (9)$$

The detection efficiencies (ε^A , ε^C and ε^{Coin}) can be found in Table 3. The average number of particles ($N_{part/pp}^A$, $N_{part/pp}^C$ and $N_{part/pp}^{Coin}$) are obtained by converting the number of hits in Table 3 into number of particles by using Equation 46 in Appendix D. The average number of pp interactions per event is obtained by numerical inversion of Equation 43 with a 10^{-10} precision:

$$\mu = f^{-1}(N_{part/BX})$$

The uncertainty on μ is evaluated as the maximum variation of μ corresponding to a $\pm 1\sigma$ variation of $N_{part/BX}$. The uncertainties on the efficiencies are neglected. The measurements of μ with the combinatorial model in hit counting are plotted against the true value in Figure 27.

5.6 Combinatorial model

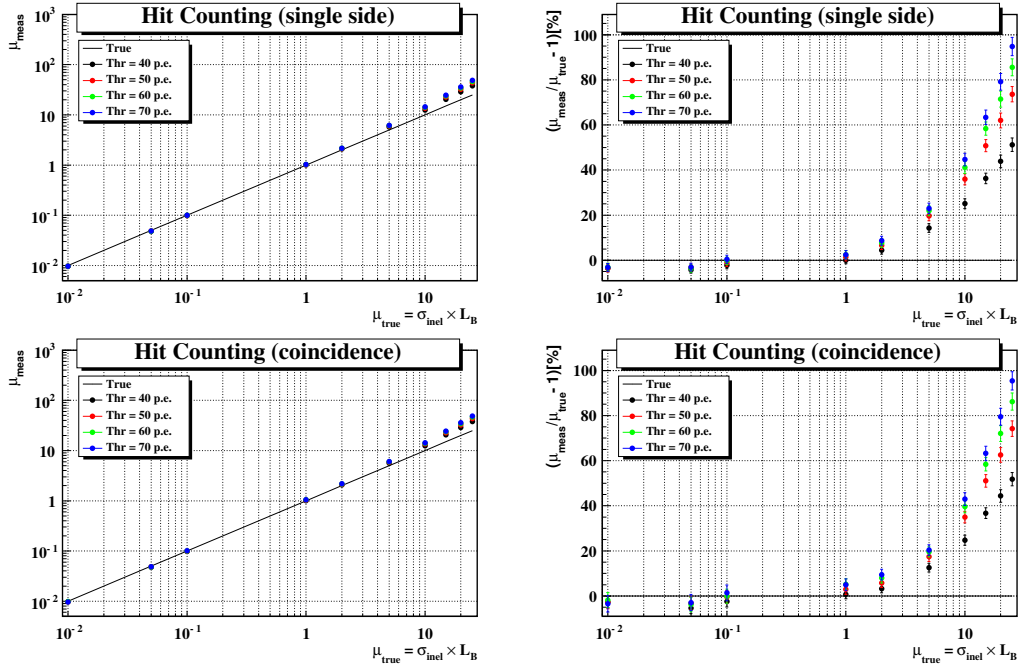


Figure 27. Left: average number of pp interactions per event measured with the combinatorial model (μ_{meas}) in hit counting single side (top) and coincidence mode (bottom) as a function of the true value (μ_{true}) for different thresholds. Right: deviation from the true value.

In both trigger modes with a 50 p.e. threshold, the difference between the measured and the true number of pp interactions is within the uncertainty (2% in single side and 3% in coincidence) when $\mu < 1$. The number of detected particles is larger than the combinatorial model prediction at large μ values due to the migration effect (see Section 5.3), therefore μ is overestimated. The deviation increases with the threshold due to an increased migration effect.

By construction, the combinatorial model in single side mode is equivalent to the linear model. The advantage of using the combinatorial model is that the accuracy in coincidence mode is at the same level of the single side mode, while the linear model in coincidence mode fails already at $\mu = 0.1$. The accuracy of the combinatorial model for $\mu < 1$ is an upper limit and can be improved by increasing the size of the calibration sample.

The results of the combinatorial model show a larger discrepancy between measured and true μ values than the linear model at large μ . This is due to the fact that the combinatorial model corrects for saturation while the linear model does not. Since the migration effect leads to an overestimate and the saturation to an underestimate, these two effects cancel to some degree in the linear model.

5.7 Polynomial fit model

5.7 Polynomial fit model

The average number of hits per event ($N_{hits/BX}$) is not linear with μ for 3 reasons:

- I - Saturation effect due to hit counting instead of particle counting;
- II - Combinatorial effects arising in coincidence mode;
- III - Migration above threshold of small signals at high μ .

The first two effects have been analytically calculated, as discussed above. The migration effect produces a consistent overestimate of μ already at $\mu = 1$ (for hit counting in coincidence mode) and has not been analytically evaluated.

The accuracy of the luminosity monitor for $\mu > 1$ can be increased by parameterizing all non-linear effects with a polynomial fit:

$$N_{hits/BX} = f(\mu) = a + b\mu + c\mu^2 + d\mu^3 + e\mu^4 + f\mu^5$$

The inverse of the fit function is used to evaluate the average number of pp interactions per event corresponding to a given number of hits at any luminosity:

$$\mu = f^{-1}(N_{hits/BX})$$

To test the performance of the polynomial fit model, the Monte Carlo sample of 9159 single pp interaction events is divided into two equal subsets. Each set is used to build 10 samples of multiple pp interaction events according to a Poissonian distribution with average $\mu_{true} = 0.01, 0.05, 0.1, 1, 2, 5, 10, 15, 20, 25$. One sample is used to perform the polynomial fit (**calibration sample**), the other is used to test the luminosity monitoring performance (**measurement sample**). Single pp interaction events are selected randomly from the calibration sample and are used twice in each measurement sample, therefore uncertainties are increased by a factor of $\sqrt{2}$.

Figure 28 shows the average number of hits per event ($N_{hits/BX}$) as a function of the number of pp interactions μ_{true} in the calibration sample. Results are shown in single side and coincidence mode with four different values of the photo-electron threshold. A third (fifth) order polynomial fit is superimposed to the plot in single side (coincidence) mode. The average deviation from the fit is 1% (2%) in single side (coincidence) mode and represents the systematic uncertainty associated to the inversion of the fit function.

Figure 29 shows the average number of pp interactions extracted from the measurement samples using the inverse of the polynomial fit. With a 50 p.e. threshold, the maximum deviation from linearity is 3% (6%) in single side (coincidence mode) mode in the full luminosity range ($\mu < 25$). Similar results are obtained by inverting calibration and measurement samples. The accuracy of the polynomial fit model can be improved by increasing the size of the calibration sample.

5.7 Polynomial fit model

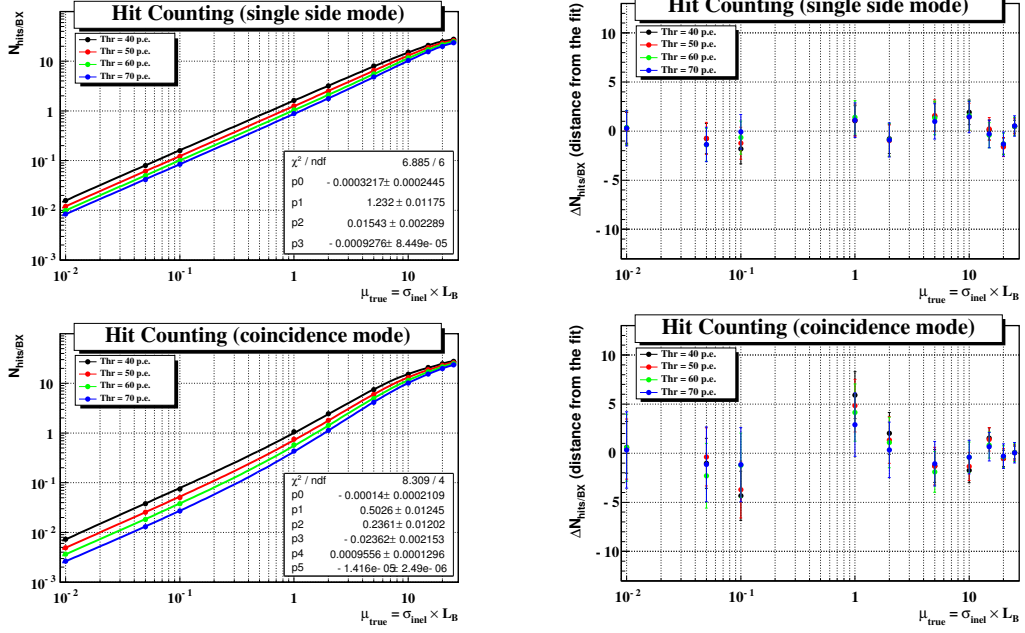


Figure 28. Polynomial fit of $N_{\text{hits}/\text{BX}}$ as a function of the true value in single side (top-left) and coincidence mode (bottom-left). The deviation from the fit is shown in the right plots.

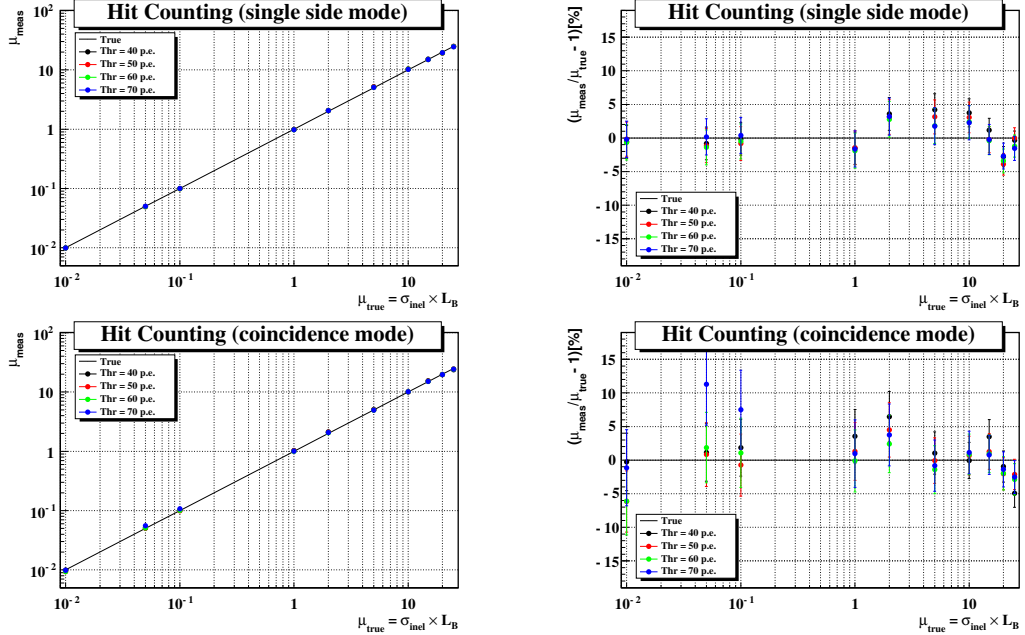


Figure 29. Comparison between the average number of pp interactions per event measured with LUCID (dots) and the prediction of the polynomial model (solid line) by counting the number of hits in single side (top-left) and coincidence mode (bottom-left). The deviation from the prediction is shown in the right plots.

6 Conclusions and summary

6 Conclusions and summary

LUCID detects charged particles in the pseudo-rapidity range [5.6, 6.2]. The light yield of primary particles in the wavelength range [160 nm, 700 nm] is predicted to be 105 *p.e.* (75 from the gas and 30 from the PMT window). With a 50 *p.e.* threshold, the probability to detect a inelastic pp collision is $(55.8 \pm 0.05)\%$ in single side mode and $(13.5 \pm 0.04)\%$ in coincidence mode. The average number of hits per pp collision is 1.21 ± 0.02 .

The performance of three models (linear, combinatorial, polynomial) to extract the average number of pp collisions per event (μ) with LUCID have been studied using 9159 events of simulated pp interactions. Two counting methods are used: in a zero counting method, μ is extracted from the number of empty events; in a hit counting method, μ is extracted from the average number of hits per event. Two detection modes are used: in single side mode, a pp interaction is detected if at least one module registers a hit; in coincidence mode, both modules must register a hit. The upper limit on the difference between the true value of μ and the measurements with the different models are reported in Table 4⁴.

Model	Counting Method	Range	$\mathcal{L}_{BX} [10^{30}cm^{-2}s^{-1}]$	σ_{sys}^{model}
Linear	Zero (single side)	$\mu < 2$	< 0.280	< 2%
Linear	Zero (coincidence)	$\mu < 0.1$	< 0.014	< 4%
Linear	Hit (single side)	$\mu < 1$	< 0.140	< 2%
Linear	Hit (coincidence)	$\mu < 0.1$	< 0.140	< 7%
Combinatorial	Zero (single side)	$\mu < 2$	< 0.280	< 2%
Combinatorial	Zero (coincidence)	$\mu < 2$	< 0.280	< 3%
Combinatorial	Hit (single side)	$\mu < 1$	< 0.140	< 2%
Combinatorial	Hit (coincidence)	$\mu < 1$	< 0.140	< 3%
Polynomial	Hit (single side)	$\mu < 25$	< 3.5	< 3%
Polynomial	Hit (coincidence)	$\mu < 25$	< 3.5	< 6%

Table 4. Systematic uncertainty of the μ extraction model when monitoring luminosity with LUCID assuming $\sigma_{pp}^{inel} = 80\text{ mb}$. For each model, the range of validity in terms of mean number of pp interactions per event (μ) and bunch luminosity (\mathcal{L}_{BX}) is shown.

For operation in coincidence mode at $\mu < 2$, the accuracy of the combinatorial model is 3% in both zero and hit counting methods. For operation up to $\mu = 25$, the only choice is the polynomial fit model which gives a 6% accuracy in the full luminosity range ($\mu < 25$). The accuracy of all models can be improved by increasing the size of the Monte Carlo calibration sample.

⁴Note that this is only one contribution to the total systematic uncertainty. Other effects are beyond the scope of this note and will become available once the machine background will be known.

A Wavelength dependent parameters

A Wavelength dependent parameters

λ [nm]	C_4F_{10} Absorption Length [m]
150	0.001
172	0.82
175	4
200	6
700	6

Table 5. Absorption Length of C_4F_{10} as a function of photon wavelength.

λ [nm]	Aluminum Reflectivity	λ [nm]	Aluminum Reflectivity
150	0.022456	450	0.923245
175	0.227736	475	0.934399
200	0.388777	500	0.943149
225	0.515113	525	0.950013
250	0.614222	550	0.955398
275	0.691972	575	0.959622
300	0.752967	600	0.962936
325	0.800817	625	0.964399
350	0.838355	650	0.967576
375	0.867803	675	0.969176
400	0.890905	700	0.970431
425	0.909028		

Table 6. Aluminum Reflectivity as a function of photon wavelength.

A Wavelength dependent parameters

λ [nm]	C_4F_{10} Quantum Efficiency	λ [nm]	C_4F_{10} Quantum Efficiency
160	0.063096	440	0.246415
170	0.152522	450	0.237137
180	0.188365	460	0.232631
190	0.211349	470	0.219617
200	0.237137	480	0.207332
210	0.232631	490	0.195734
220	0.223872	500	0.177828
230	0.207332	510	0.161560
240	0.203392	520	0.146780
250	0.199526	530	0.133352
260	0.192014	540	0.125893
270	0.188365	550	0.114376
280	0.192014	560	0.101937
290	0.207332	570	0.077923
300	0.211349	580	0.055165
310	0.215443	590	0.044668
320	0.223872	600	0.036869
330	0.228209	610	0.029854
340	0.232631	620	0.021962
350	0.237137	630	0.017113
360	0.241732	640	0.012115
370	0.246415	650	0.008912
380	0.256055	660	0.005623
390	0.251189	670	0.003687
400	0.251189	680	0.002073
410	0.251189	690	0.001188
420	0.251189	700	0.000764
430	0.246415		

Table 7. Hamamatsu R762 PMT Quantum Efficiency as a function of photon wavelength.

B Counting empty events

B Counting empty events

Single side mode

The probability of having an empty event ($P_{0/BX}$) in single side mode is given by two contributions:

I - probability of having 0 interactions;

II - probability of having n interactions with 0 hits in both modules.

Assuming that interactions are Poissonian, Term I can be written as:

$$I = P_\mu(0) = \frac{e^{-\mu}\mu^0}{0!} = e^{-\mu} \quad (10)$$

Under the assumption that the probability to detect an interaction does not depend on the number of interactions in a given event, the combined probability of not detecting n interactions in a event (Term II) can be written as:

$$II = (1 - \varepsilon^{Sing})^n \quad (11)$$

where ε^{Sing} is the probability to detect an interaction in single side mode. This assumption is true only to a first approximation. In reality being the hit detection dependent on an photoelectron threshold, if n interactions are present in an event, the probability to see $n + 1$ interactions is larger due to the migration effect (see Section 5.3).

Term II is convoluted with a Poissonian distribution of average μ (the sum starts from $n = 1$ to avoid double counting of Term I):

$$\sum_{n=1}^{\infty} (1 - \varepsilon^{Sing})^n \frac{e^{-\mu}\mu^n}{n!} = \sum_{n=0}^{\infty} (1 - \varepsilon^{Sing})^n \frac{e^{-\mu}\mu^n}{n!} - e^{-\mu} = e^{-\varepsilon^{Sing}\mu} - e^{-\mu} \quad (12)$$

The probability of observing an empty event is the sum of Equations 10 and 12:

$$P_{0/BX} = e^{-\mu} + e^{-\varepsilon^{Sing}\mu} - e^{-\mu} = e^{-\varepsilon^{Sing}\mu} \quad (13)$$

This formula is obtained under the assumption that the probability of having n interactions does not change in time. For this reason luminosity will be extracted separately for each filled bunch in a sufficiently small time period (*LumiBlock*).

B Counting empty events

Coincidence mode

The probability of having an empty event in coincidence mode is the sum of four contributions:

- I - probability of having 0 interactions;
- II - probability of having n interactions with at least one interaction detected in module A, together with any number of interactions which are not detected in both modules;
- III - probability of having n interactions with at least one interaction detected in module C, together with any number of interactions which are not detected in both modules.
- IV - probability of having n interactions with 0 hits in both modules.

Assuming that interactions are Poissonian, Term I can be written as:

$$I = P_\mu(0) = \frac{e^{-\mu}\mu^0}{0!} = e^{-\mu} \quad (14)$$

To evaluate contributions II, III and IV, *exclusive* efficiencies to detect a interaction ($\varepsilon_1, \varepsilon_2, \varepsilon_3$ and ε_0) are defined in Table 8.

ε_1	probability of detecting an interaction in A, but not in C
ε_2	probability of detecting an interaction in C, but not in A
ε_3	probability of detecting an interaction in both modules
ε_0	probability of detecting no interactions ($=1 - \varepsilon_1 - \varepsilon_2 - \varepsilon_3$)

Table 8. Efficiencies needed for zero counting method in coincidence mode.

Exclusive efficiencies in Table 8 are related to the *inclusive* ones defined in Table 3 according to the formula:

$$\begin{aligned} \varepsilon_1 &= \varepsilon^A - \varepsilon^{Coin} \\ \varepsilon_2 &= \varepsilon^C - \varepsilon^{Coin} \\ \varepsilon_3 &= \varepsilon^{Coin} \\ \varepsilon_0 &= 1 - \varepsilon^A - \varepsilon^C + \varepsilon^{Coin} \end{aligned} \quad (15)$$

The calculation of Terms II, III and IV are performed under the same assumptions done in the previous section (efficiencies are constant in time and no migration effect).

B Counting empty events

Term II (III) consists of all permutations of k interactions detected in module A (C) and $n - k$ interactions not detected in any module:

$$II = \sum_{k=1}^n \varepsilon_1^k \varepsilon_0^{n-k} \binom{n}{k} = (\varepsilon_1 + \varepsilon_0)^n - \varepsilon_0^n \quad (16)$$

$$III = \sum_{k=1}^n \varepsilon_2^k \varepsilon_0^{n-k} \binom{n}{k} = (\varepsilon_2 + \varepsilon_0)^n - \varepsilon_0^n \quad (17)$$

Term IV is the probability of having an event with n interactions which are not detected neither by any single module nor by the both modules together:

$$IV = \varepsilon_0^n \quad (18)$$

Terms II, III and IV are convoluted with a Poissonian distribution with a average μ (the sum starts from $n = 1$ to avoid double counting of Term I):

$$\sum_{n=1}^{\infty} \frac{e^{-\mu} \mu^n}{n!} [(\varepsilon_1 + \varepsilon_0)^n - \varepsilon_0^n] = e^{-\mu} [e^{-\mu(\varepsilon_1+\varepsilon_0)} - e^{\mu\varepsilon_0}] \quad (19)$$

$$\sum_{n=1}^{\infty} \frac{e^{-\mu} \mu^n}{n!} [(\varepsilon_2 + \varepsilon_0)^n - \varepsilon_0^n] = e^{-\mu} [e^{-\mu(\varepsilon_2+\varepsilon_0)} - e^{\mu\varepsilon_0}] \quad (20)$$

$$\sum_{n=1}^{\infty} \frac{e^{-\mu} \mu^n}{n!} \varepsilon_0^n = e^{-\mu}(e^{\mu\varepsilon_0} - 1) \quad (21)$$

The total probability of observing an empty event is the sum of Equations 14, 19, 20 and 21:

$$P_{0/BX} = e^{-\mu(1-\varepsilon_0-\varepsilon_1)} + e^{-\mu(1-\varepsilon_0-\varepsilon_2)} - e^{-\mu(1-\varepsilon_0)} \quad (22)$$

Given the relations in Table 8, Equation 22 can be written as:

$$P_{0/BX} = e^{-\mu\varepsilon^A} + e^{-\mu\varepsilon^C} - e^{-\mu(\varepsilon^A + \varepsilon^C - \varepsilon^{Coin})} \quad (23)$$

C Counting particles in coincidence mode

C Counting particles in coincidence mode

In coincidence mode, there are two possibilities to detect an event with multiple interactions. A *true* coincidence occurs when at least one interaction is detected simultaneously in both modules. A *fake* coincidence occurs when no interaction is detected simultaneously in both modules, but at least two interactions are separately detected in different modules.

In coincidence mode, the average number of detected particles in events with n interactions is the sum of two contributions:

- I - the event contains at least one interaction which is detected in both modules, together with any number of interactions which are only detected in module A and not in C, and vice versa;
- II - the event contains 0 interactions detected in both modules, together with at least one interaction which is only detected in module A and one which is only detected in module C.

The average number of particles corresponding to Terms I and II is the sum of the probability of each configuration times the corresponding number of detected interactions, times the number of particles per detected interaction.

Four *exclusive* definitions of average number of particles in the whole detector per detected interaction are used (Table 10).

C_1	no. of particles per detected interaction in A, but not in C
C_2	no. of particles per detected interaction in C, but not in A
C_3	no. of particles per detected interaction in both modules
C_4	no. of particles per detected interaction in any module, not in both

Table 9. Exclusive definitions of average number of particles.

The probability of each configuration is evaluated by using the efficiencies to detect an interaction defined in Table 8 (ε_1 , ε_2 , ε_3 and ε_0), together with the efficiency to detect an interaction in any module, but not in both (ε_4).

Suppose n interactions occurred in an event, Terms I and II can be written as:

$$I = \sum_{k=1}^n \varepsilon_3^k \binom{n}{k} \left[\sum_{l=0}^{n-k} \varepsilon_4^l (1 - \varepsilon_4 - \varepsilon_3)^{n-k-l} \binom{n-k}{l} \right] [kC_3 + lC_4] \quad (24)$$

$$II = \sum_{k=1}^n \varepsilon_1^k \binom{n}{k} \left[\sum_{l=1}^{n-k} \varepsilon_2 \varepsilon_0^{n-k-l} \binom{n-k}{l} \right] [kC_1 + lC_2] \quad (25)$$

C Counting particles in coincidence mode

Term I The first contribution consists of k interactions detected in both modules, l of the remaining $n - k$ interactions detected in only one module and the remaining $n - k - l$ interactions undetected.

The probability of detecting k interactions in both modules is ε_3^k . The probability of detecting l interactions in only one module is ε_4^l . The probability of not detecting $n - k - l$ interactions is $(1 - \varepsilon_4 - \varepsilon_3)^{n-k-l}$.

Binomial factors are used to account for all permutations of k out of n interactions and l out of $n - k$ interactions.

The average number of particles given by k interactions detected in both modules is kC_3 , while that of l interactions detected in one module is lC_4 .

Term II The second contribution consists of k interactions detected in module A but not in C, l of the remaining $n - k$ interactions detected in module C but not in A, and the remaining $n - k - l$ interactions undetected.

The probability of detecting k interactions in module A is ε_1^k . The probability of detecting l interactions in module C is ε_2^l . The probability of not detecting $n - k - l$ interactions is ε_0^{n-k-l} .

Binomial factors are used to account for all permutations of k out of n interactions and l out of $n - k$ interactions.

The average number of particles given by k interactions detected in both modules is kC_1 , while that of l interactions detected in one module is lC_2 .

Sum over l The l -sums in Equations 24 and 25 can be evaluated by means of the binomial theorem:

$$kC_3 \sum_{l=0}^{n-k} \varepsilon_4^l (1 - \varepsilon_4 - \varepsilon_3)^{n-k-l} \binom{n-k}{l} = kC_3 (1 - \varepsilon_3)^{n-k} \quad (26)$$

$$C_4 \sum_{l=0}^{n-k} l \varepsilon_4^l (1 - \varepsilon_4 - \varepsilon_3)^{n-k-l} \binom{n-k}{l} = C_4 (n-k) \varepsilon_4 (1 - \varepsilon_3)^{n-k-1} \quad (27)$$

$$kC_1 \sum_{l=1}^{n-k} \varepsilon_2^l \varepsilon_0^{n-k-l} \binom{n-k}{l} = kC_1 [(\varepsilon_0 + \varepsilon_2)^{n-k} - \varepsilon_0^{n-k}] \quad (28)$$

$$C_2 \sum_{l=1}^{n-k} l \varepsilon_2^l \varepsilon_0^{n-k-l} \binom{n-k}{l} = C_2 (n-k) \varepsilon_2 (\varepsilon_0 + \varepsilon_2)^{n-k-1} \quad (29)$$

C Counting particles in coincidence mode

Sum over k Equations 26-29 are used to evaluate the k -sums in Equations 24 and 25 by means of the binomial theorem:

$$C_3 \sum_{k=1}^n k \varepsilon_3^k (1 - \varepsilon_3)^{n-k} \binom{n}{k} = C_3 \varepsilon_3 n \quad (30)$$

$$C_4 \varepsilon_4 \sum_{k=1}^n n \varepsilon_3^k (1 - \varepsilon_3)^{n-k-1} \binom{n}{k} = C_4 \varepsilon_4 n \left[\left(\frac{1}{1 - \varepsilon_3} \right) - (1 - \varepsilon_3)^{n-1} \right] \quad (31)$$

$$-C_4 \varepsilon_4 \sum_{k=1}^n k \varepsilon_3^k (1 - \varepsilon_3)^{n-k-1} \binom{n}{k} = -C_4 \varepsilon_4 n \frac{\varepsilon_3}{1 - \varepsilon_3} \quad (32)$$

$$C_1 \sum_{k=1}^n k \varepsilon_1^k (\varepsilon_0 + \varepsilon_2)^{n-k} \binom{n}{k} = C_1 \varepsilon_1 n (\varepsilon_0 + \varepsilon_1 + \varepsilon_2)^{n-1} \quad (33)$$

$$-C_1 \sum_{k=1}^n k \varepsilon_1^k \varepsilon_0^{n-k} \binom{n}{k} = -C_1 \varepsilon_1 n (\varepsilon_0 + \varepsilon_1)^{n-1} \quad (34)$$

$$C_2 \varepsilon_2 \sum_{k=1}^n n \varepsilon_1^k (\varepsilon_0 + \varepsilon_2)^{n-k-1} \binom{n}{k} = C_2 \varepsilon_2 n \left[\frac{(1 - \varepsilon_3)^n}{\varepsilon_0 + \varepsilon_2} - (\varepsilon_0 + \varepsilon_2)^{n-1} \right] \quad (35)$$

$$-C_2 \varepsilon_2 \sum_{k=1}^n k \varepsilon_1^k (\varepsilon_0 + \varepsilon_2)^{n-k-1} \binom{n}{k} = -C_2 \varepsilon_2 n \varepsilon_1 \frac{(1 - \varepsilon_3)^{n-1}}{\varepsilon_0 + \varepsilon_2} \quad (36)$$

Sum of Terms I and II Given that $C_1 \varepsilon_1$ is the number of particles registered in the whole detector when the interaction is detected in module A only and $C_2 \varepsilon_2$ is the number of particles registered in the whole detector when the interaction is detected in module C only, the sum of these Terms gives the number of particles registered in the whole detector when the interaction is detected in module A or in module C but not in both ($C_4 \varepsilon_4$):

$$C_4 \varepsilon_4 = C_1 \varepsilon_1 + C_2 \varepsilon_2 \quad (37)$$

Using Equation 37, the sum of Equations 30-36 gives:

$$I + II = C_3 \varepsilon_3 n + C_1 \varepsilon_1 n [1 - (\varepsilon_0 + \varepsilon_1)^{n-1}] + C_2 \varepsilon_2 n [1 - (\varepsilon_0 + \varepsilon_2)^{n-1}] \quad (38)$$

C Counting particles in coincidence mode

Poissonian sum The average number of particles per event is given by the convolution of Equation 38 with a Poissonian with average μ :

$$N_{part/BX} = \sum_{n=0}^{\infty} (I + II) \frac{e^{-\mu} \mu^n}{n!} \quad (39)$$

Given the relations:

$$\sum_{n=0}^{\infty} n \frac{e^{-\mu} \mu^n}{n!} = \mu \quad \text{and} \quad \sum_{n=0}^{\infty} \frac{k^n}{n!} = e^k \quad (40)$$

Equation 39 becomes:

$$N_{part/BX} = C_3 \varepsilon_3 \mu + C_1 \varepsilon_1 \mu [1 - e^{-\mu(\varepsilon_2 + \varepsilon_3)}] + C_2 \varepsilon_2 \mu [1 - e^{-\mu(\varepsilon_1 + \varepsilon_3)}] \quad (41)$$

The *inclusive* average numbers of particles are defined in Table 10.

N_{part/pp^*}^A	no. of particles per interaction detected in A (regardless of C)
N_{part/pp^*}^C	no. of particles per interaction detected in C (regardless of A)
N_{part/pp^*}^{Coin}	no. of particles per interaction detected in both modules

Table 10. Inclusive definitions of average number of particles.

Using relation 15 and the following ones:

$$\begin{aligned} C_1 \varepsilon_1 &= N_{part/pp^*}^A \varepsilon^A - N_{part/pp^*}^{Coin} \varepsilon^{Coin} = N_{part/pp}^A - N_{part/pp}^{Coin} \\ C_2 \varepsilon_2 &= N_{part/pp^*}^C \varepsilon^C - N_{part/pp^*}^{Coin} \varepsilon^{Coin} = N_{part/pp}^C - N_{part/pp}^{Coin} \end{aligned} \quad (42)$$

Equation 41 can be written as:

$$\begin{aligned} N_{part/BX} &= \mu N_{part/pp}^{Coin} + \\ &\quad \mu \left(N_{part/pp}^A - N_{part/pp}^{Coin} \right) \left(1 - e^{-\mu \varepsilon^C} \right) + \\ &\quad \mu \left(N_{part/pp}^C - N_{part/pp}^{Coin} \right) \left(1 - e^{-\mu \varepsilon^A} \right) \end{aligned} \quad (43)$$

D From hits to particles

The way particles are distributed among the tubes depends on the dynamics of the interactions: non diffractive, single- and double-diffractive. Assuming that particles are spread uniformly over the detector⁵, the average number of particles hitting one tube is N_{part}/N_{tubes} , where N_{part} is the total number of detected particles.

Assuming that particles are distributed according to a Poissonian, the probability to have at least one particle in a tube, namely a hit, is:

$$1 - e^{-\frac{N_{part}}{N_{tubes}}} \quad (44)$$

Such probability is turned into number of hits with the following formula:

$$N_{hits} = N_{tubes} \left[1 - e^{-\frac{N_{part}}{N_{tubes}}} \right] \quad (45)$$

Equation 45 allows one to extract the number of particles crossing the detector from the number of hits by using the following relation:

$$N_{part} = -N_{tubes} \log \left(1 - \frac{N_{hits}}{N_{tubes}} \right) \quad (46)$$

⁵Figure 21 shows that this assumption is verified to a good extent.

REFERENCES

References

- [1] S. De Capua *et al.*, Il Nuovo Cimento **123 B** (2008) 423.
- [2] S. Ask, *Simulation of luminosity monitoring in atlas*, ATL-LUM-PUB-2006-001.
- [3] G. Aad *et al.*, JINST **3** (2008) S08003.
- [4] ATLAS TDR 018, CERN/LHCC 2008-04.
- [5] S. Agostinelli *et al.*, NIM **A506** (2003) 250.
- [6] Hamamatsu private communication.
- [7] J. D. Jackson, *Classical Electrodynamics*, Wiley & Sons, 1975.
- [8] R. Arnold *et al.*, NIM **A270** (1988) 289.
- [9] <http://en.wikipedia.org>.
- [10] <http://geant4.cern.ch/G4UsersDocuments/UsersGuides/PhysicsReferenceManual>.
- [11] W. R. Leo, *Techniques for Nuclear and Particle Physics Experiments*, Springer, 1987.
- [12] R. Engel, *Phojet manual*, <http://www-ik.fzk.de/~engel/phojet.html>.
- [13] <http://www.staff.uni-mainz.de/zeitnitz/G calor/g calor.html>.
- [14] G. A. Schuler and T. Sjostrand, Phys. Rev. **D49** (1994) 2257.
- [15] T. Sjostrand *et al.*, hep-ph/0603175.
- [16] W. Bell, ATL-PHYS-PROC-2009-051; ATL-COM-PHYS-2009-156.
- [17] G. Aad *et al.*, arXiv:0901.0512v4.
- [18] S. Baranov *et al.*, ATL-GEN-2005-001.